THESIS APPROVAL

GRADUATE SCHOOL, KASETSART UNIVERSITY

Master of Engineering (Information and Communication Technology for Embedded Systems)

DEGREE

Information and Communication Technology for Embedded Systems — **FIELD**

Electrical Engineering — **DEPARTMENT**

TITLE: A Design of A MEMS Based Confocal Probe for Multiple Wavelengths

NAME: Mr. Techaniti Chantakien

THIS THESIS HAS BEEN ACCEPTED BY

_____ **THESIS ADVISOR**

(Mr. Pisut Raphisak, Ph.D.)

_____ **THESIS CO-ADVISOR**

(Professor Wibool Piyawatthanametha, Ph.D.)

_____ **THESIS CO-ADVISOR**

(Professor Ituso Kumazawa, Dr.Eng.)

_____ **DEPARTMENT HEAD**

(Associate Professor Teerasit Kasetkasem, Ph.D.)

APPROVED BY THE GRADUATE SCHOOL ON _____

_____ **DEAN**

(Associate Professor Gunjana Theeragool, D.Agr.)

THESIS

A DESIGN OF A MEMS BASED CONFOCAL PROBE FOR MULTIPLE WAVELENGTHS

TECHANITI CHANTAKIEN

A Thesis Submitted in Partial Fulfillment of
the Requirements for the Degree of
Master of Engineering (Information and Communication T chnology for Embedded Systems)
Graduate School, Kasetsart University
2012

Techaniti Chantakien 2012: A Design of A MEMS Based Confocal Probe for Multiple Wavelengths. Master of Engineering (Information and Communication Technology for Embedded Systems), Major Field: Information and Communication Technology for Embedded Systems, Department of Electrical Engineering. Thesis Advisor: Mr. Pisut Raphisak, Ph.D. 62 pages.

The performance of the microelectromechanical systems (MEMS) based single axis confocal microscope is greatly limited due to chromatic aberration when it is used with multiple wavelengths and nonlinearity MEMS scanner's operation. The purpose of this study, there are two purposes, is to reduce chromatic aberration in a single axis confocal microscope probe for multiple wavelengths. Another purpose of this study is to propose a method to linearize the scanning field in open-loop operation.

To reduce chromatic aberration in single axis confocal microscope probe, the achromatic lenses which are designed to reduce the effects of chromatic aberration are used as beam expander and objective lens. To linearize scanning field, the utilization of Radial Basis Function (RBF) neural networks to control MEMS scanner are proposed. The Radial Basis Function neural networks are created from data sets archived from MEMS scanner's characteristic imulation. However, the accuracy of RBF neural network depends on hidden node. Therefore, RBF neural network's performance is measured via mean squared error value. From the experiment, the RBF neural networks which have mean squared error less than 0.05 can be used to control MEMS scanner in MEMS based sing axis confocal microscope.

_____ _____ __ / __ / __

Student's signature Thesis Advisor's signature

ACKNOWLEDGEMENTS

I would like to grateful thank and deeply indebted to Pisut Raphisak my thesis advisor, Dr. Wibool Piyawattanametha my co-advisors from National Electronics and Computer Technology Center, and Prof. Itsuo Kumazawa my co-advisor from Tokyo Institute of Technology for advice, encouragement and valuable suggestion for completely writing of thesis.

This research is financially supported by Thailand Advanced Institute of Science and Technology - Tokyo Institute of Technology (TAIST-Tokyo Tech), National Science and Technology Development Agency (NSTDA), Tokyo Institute of Technology (Tokyo Tech), National Research Council of (NRCT) and Kasetsart University (KU).

Techaniti Chantakien

January 2012

TABLE OF CONTENTS

Page

TABLE OF CONTENTS	i
LIST OF TABLES	ii
LIST OF FIGURES	iii
LIST OF ABBREVIATIONS	vi
INTRODUCTION	1
OBJECTIVES	7
LITERATURE REVIEW	8
MATERIALS AND METHODS	20
Materials	20
Methods	20
RESULTS AND DISCUSSION	49
Results	49
Discussion	54
CONCLUSION AND RECOMMENDATION	55
Conclusion	55
Recommendation	56
LITERATURE CITED	57
CIRRICULUM VITAE	62

LIST OF TABLES

Table		Page
1	Parameters of 2D MEMS scanner	29
2	Relationship of actuation voltage and the position of spot on image plane	35

LIST OF FIGURES

Figure		Page
1	Schematic of a confocal laser scanning microscope	1
2	The various forms of scanning optical microscopes	2
3	The depth discrimination of confocal laser scanning microscope	3
4	The variation in detected signal as a plane mirror is scanned axially through focus	4
5	Variety of applications of MEMS scanner	5
6	Result of decreasing diameter of objective lens in SAC architecture	9
7	Light schematic of DAC architecture	10
8	Various designs of MEMS based SAC microscope probe	11
9	Schematic of single fiber confocal microscope system	12
10	Raster scanning	13
11	Image from raster scanning	14
12	Calculated Lissajous scan patterns	15
13	Schematic of MEMS based vector scanning system	16
14	Comparison between parallel-plate and vertical comb-drive actuators	17
15	Methodology of differential the bias voltage	18
16	Scheme of the linearization by RBF neural network	19
17	Configuration of MEMS based single axis confocal microscope	22
18	Configuration of Keplerian telescope	22
19	Focusing the off-axis laser beam on the image plane	23

LIST OF FIGURES (Continued)

Figure		Page
20	Property of Achromatic doublet lens	24
21	Schematic of a miniature single axis confocal microscope probe for multiple wavelengths	25
22	Spot diagram	25
23	MTF graph	26
24	Focal shift graph	27
25	Displacement distance from center versus light deflected angle	28
26	Schematic of the 2D AVC scanner	29
27	The capacitance per unit length versus the finger offset	31
28	Movable comb finger	32
29	DC scanning characteristic of a 2D AVC MEMS scanner	34
30	Light's schematic and image plane	34
31	Optical system modeling	36
32	Displacement distance of spot on image plane	37
33	Schematic of the linearization with RBF neural network	38
34	Linear relationship of controlling voltages and displacement of spot on image plane	39
35	Radial Basis Function Neural Network architecture	40
36	Radial Basis neural network in MATLAB	42
37	Training data set creation	43
38	Comparison graph between output from analytical and output from neural network for inner mirror	44

LIST OF FIGURES (Continued)

Figure		Page
39	Comparison graph between output from analytical calculation and output from neural network for outer frame	46
40	Point spread function of two illumination points separated with Rayleigh distance	48
41	Test process diagram	50
42	The distance error of for inner mirror	52
43	The distance error of outer frame	53

LIST OF ABBREVIATIONS

APD	=	Avalanche Photodiode
DAC	=	Dual Axis Confocal
DC	=	Direct Current
FOV	=	Field of View
FWHM	=	Full Width Half Maximum
MEMS	=	Microelectromechanical systems
MSE	=	Mean Square Error
MTF	=	Modulation Transfer Function
NA	=	Numerical Aperture
NN	=	Neural Network
OTF	=	Optical Transfer Function
PSB	=	Polarizing Beamsplitter
PSD	=	Photo Sensing Detector
QWP	=	Quarter Wave Plate
S	=	Sagittal
SAC	=	Single Axis Confocal
T	=	Tangential
WD	=	Working Distance
2D	=	Two dimensions

A DESIGN OF A MEMS BASED CONFOCAL PROBE FOR MULTIPLE WAVELENGTHS

INTRODUCTION

There has been variety of reasons for the growth of interest in confocal laser scanning microscopy during last decade years. In essence, the confocal microscope offers the chance to image thick biological tissue in three dimensions. This instrument operates well in the bright-field and fluorescence mode. The early section of introductory chapter we will explain a very simple principle which will allow us to understand the main aspects of confocal laser scanning microscopy. Then, we will consider microelectromechanical systems (MEMS) scanner. It will be used with confocal laser scanning microscope probe for scaling down the confocal laser scanning microscope to handheld size.

1. Confocal Laser Scanning Microscope

The conventional microscope is a parallel processing system which images the entire object field simultaneously. This is a serve requirement for the optical components. If we no longer try to image the whole object at once, we can relax this requirement. The limit of the relaxation is to image of only one object point at a time. A typical confocal laser scanning microscope is shown Figure 1. The essential components are mechanism for scanning the laser beam relative to the specimen and appropriate photodetectors to collect the reflected or transmitted light.

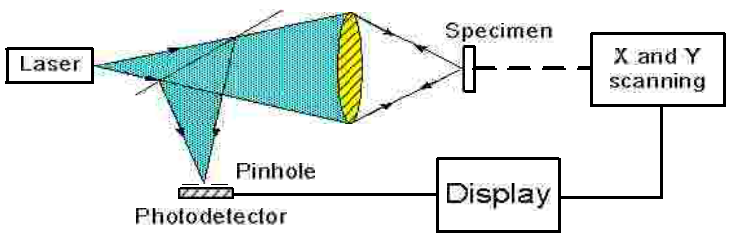

Figure 1 Schematic of a confocal laser scanning microscope.

The key elements of the optical system of a conventional optical microscope are illustrated Figure 2(a). In essence, the object is illuminated by a patch of light from an extended source via a condenser lens. The illuminated object is then imaged by the objective lens into the image plane. In this case the resolution results from only the objective lens. A scanning microscope could be built by scanning a point detector through the image plane to measure the image intensity of each object point, Figure 2(b). In this way we would build up an image point by oint, which could be stored in a computer and displayed on a screen. An analogous optical system is shown in Figure 2(c), which uses a point source and a large area detector. Here the objective lens probes the specimen, point by point, with a finely focused spot of light. This collector lens is analogous to the condenser lens in conventional microscope, and thus plays a minor role in determining resolution.

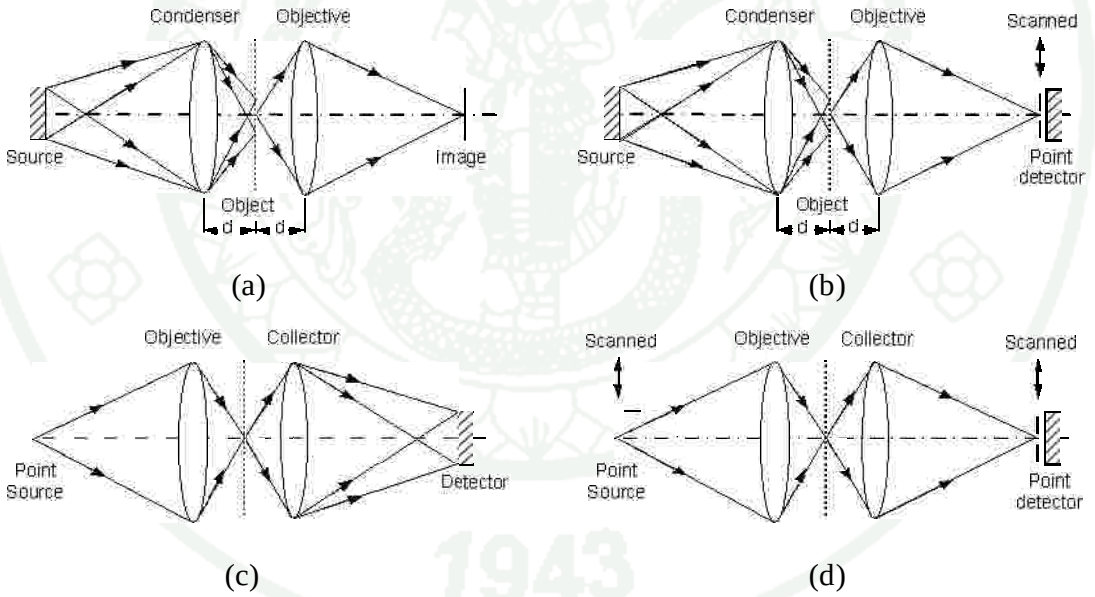

Figure 2 The various forms of scanning optical microscopes from (Corle and Kino, 1996) (a) Conventional microscope, (b) A conventional scanning microscope, (c) A conventional scanning microscope, (d) The confocal optical system.

In order to make the second lens contribute to the resolution, collector lens need to act as imaging lens. It can be archived by using a point detector rather than a large area detector. This is the form of the confocal scanning microscope, Figure 2(d). Here light from the point source probes a very small region of the object, and the point detector ensures that only light from that same is detected. In the figure, an image is built up by scanning the source and detector synchronism. In practice, it may prove more convenient to scan the light beam or the object rather than the detector and also to operate the system in reflection (Dickensheets 2001; Knittel *et al.*, 2001; Dwyer *et al.*, 2006).

The optical sectioning or depth discrimination capability become the major advantage for using confocal laser scanning microscope (Ode 1994). Principle of optical sectioning can be explained by Figure 3, where a reflection mode of confocal laser scanning microscope images a specimen with rough surface.

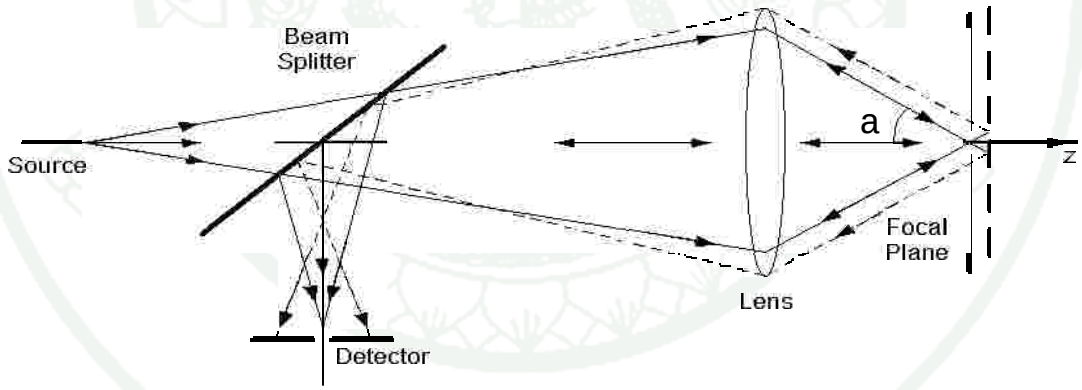

Figure 3 The depth discrimination of confocal laser scanning microscope in (Corle and Kino, 1996).

The solid lines show the optical paths when an object lies in the focal plane. At an out of scan position, the object surface supposed to be located in the plane of the vertical dashed line. In this case, simply optical ray tracing shows that the light reflected back to the detector pinhole arrives as a defocused light and is rejected out. Therefore, only the central portion of detector pinhole is detected and contributes to the image. In this way the system discriminates aga features which do not lie

within the focal region. A very simple method of both onstrating the effect and giving a measure of its strength is to scan a perfect axially through focus and measure the detected signal strength (Wilson and Carlini, 1987). Figure 4 shows a typically axial response of confocal laser scanning microscope.

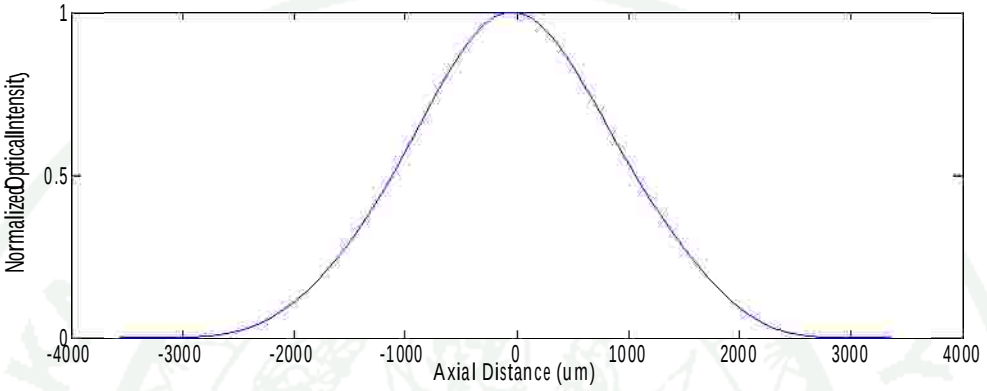

Figure 4 The variation in detected signal as a plane mirror is scanned axially through focus in (Chantakien *et al.*, 2011).

2. Microelectromechanical Systems (MEMS) Scanner

A MEMS scanner or micromirror can be defined as an actuator which is designed for light deflection. This device is a small which cannot be manufactured by processes of precision engineering. Instead, MEMS processes are preferably used, which are known from the fabrication of microelectronical devices or derived from such processes (Hah *et al.*, 2004; Carr *et al.*, 2005; Chung and Chen, 2005). Nowadays, the suitability of MEMS scanner has been dem ge variety of applications like barcode scanning (Kiang *et al.*, 1996), displays (Yamada and Kuriyama, 1998; Hagelin and Solgaard, 1999), or confocal laser scanning microscope (Hofmann *et al.*, 1999). Further applications of MEMS scanner are laser marking devices, laser printers, optical inspection systems or pico-projector (Milanovic, 2007).

Picture from: http://serialio.com/products/scanner/LaserChampBT.php and
http://www.cameraphonesplaza.com/picop-display-engine-for-projecting-images/

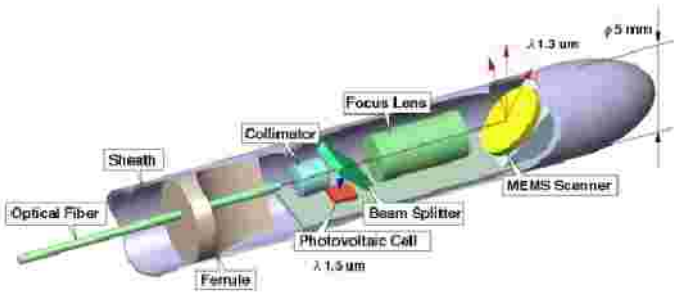

Picture from: http://www.santec.com/cn/about/coretechnology/mems

Figure 5 Variety of applications of MEMS scanner.

Because the electrostatic force is highly efficiency in micro-structure (Trimmer, 1989) so that many research afford to produce electrostatic scanner without external component and additional materials but used in standard IC-processes. Finally, the development of MEMS scanners with vertical combdrive actuators enables two dimensions (2D) MEMS scanners size to be in millimeter scale. Furthermore, 2D MEMS scanners can archive fast responses that enable high-speed transverse scanning. These two benefits allow a 2D MEMS scanner to commonly be used for confocal laser scanning microscope.

3. Problem Statement

In medical treatment, a confocal laser scanning microscope is used to image specimen or *in-vivo* applications. Sometime, the users need to use confocal laser scanning microscope with multiple wavelengths to investigate more detail. However, the image will be distorted by chromatic aberration due to properties of lens.

Moreover, a miniature confocal laser scanning microscope is the cooperation between MEMS scanner and a miniature confocal probe. But MEMS scanner displacement corresponding to driving voltage is large nonlinear which makes the control of precise positioning difficult.

The aim of this thesis is to tackle chromatic aberration on a miniature confocal probe with multiple wavelengths and nonlinearity of scanning field due to MEMS scanner operation.

OBJECTIVES

1. To design and characterize a miniature single axis confocal microscope probe for multiple wavelengths.

2. To find the relationship between MEMS scanner scanning angles and position of spot on scanning field.

3. To control and linearize the scanning field by using Radial Basis Function (RBF) neural network (NN).

LITERATURE REVIEW

The advancement in micro-lenses and MEMS scanner fabrication has resulted in the development of optical instruments including compatible confocal laser scanning microscope with high resolution. This chapter will present the detail of literature review about MEMS based confocal microscope, principle of MEMS scanner's scanning scheme, and scanning linearization. In section 1, two major types of confocal microscope are discussed. In section 2, some designs of MEMS based confocal microscope are reviewed. In section 3, the implementation of raster scanning, Lissajous scanning, and Vector scanning to MEMS scanner will be presented. Finally, section 4 will discuss the lineari ion approach of MEMS scanner.

1. Confocal Microscope

This section describes two major types of confocal microscope those are single axis confocal (SAC) microscope and dual axis confocal (DAC) microscope.

1.1 Single Axis Confocal Microscope

Single axis confocal architecture locates pinhole and lens along one main optical axis. In order to achieve high resolution and maximum light collection, a high numerical aperture (NA) objective lens is used for both light illumination and light collection. The intention to scale down the dimension this instrument to be a compatible confocal microscope, the diameter of the objective lens must be reduced to millimeter scale. As a result, the working distance (WD) as well as the field of view (FOV) is also decreased, as shown by the progression of t 3 different objectives lens in Figure 6.

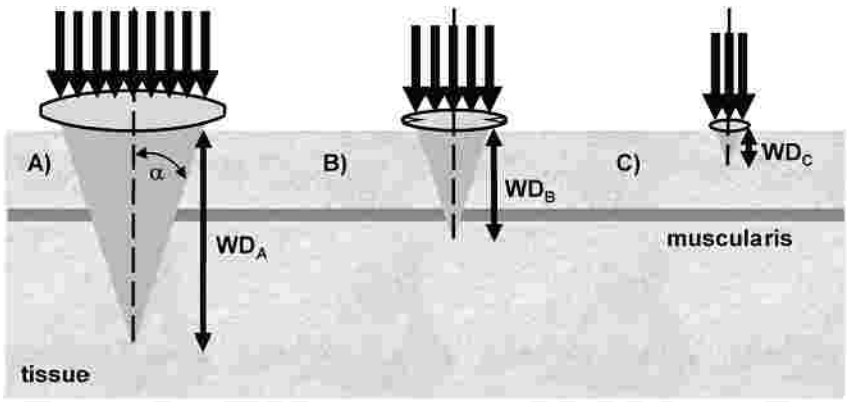

Figure 6 Result of decreasing diameter of objective lens in SAC architecture in (Chu *et al.*, 2010).

For SAC architecture, the transverse, ? r_s, and axial, ? z_s, resolution, measuring the region of full width half maximum (FWHM) spot with Gaussian beam can be calculated by the following equations:

$$\Delta r_s = \frac{0.37\lambda}{NA}; \quad \Delta z_s = \frac{1.4\lambda}{NA^2} \tag{1}$$

where *?* is the wavelength, *n* is the refractive index, *a* is the maximum convergence half-angle of the beam, *NA=n*sin*a is the numerical aperture, and sina˜ a for low NA lenses. Above equation implies that the transverse and axial resolution varies as 1/NA and $1/NA^2$, respectively. The SAC architecture can be reduced to the millimeter scale for *in vivo* imaging, but will limit the resolution, FOV, and WD due to the capability of objective lens.

1.2 Dual Axis Confocal Microscope

The dual axes confocal architecture is depicted in Figure 7. Two optical fibers oriented along separate optical axis of different low objectives lenses to spatially separate the light paths between illumination and collection. The focal volume is defined by overlap region of these two laser beams (crossed a half angle *?* from the midline). A very low probability exists for light scattered by sample along the illumination path (blue cone) to enter the low NA collection objective (green cone), thus significant improvement in the dynamic range of detection can be achieved.

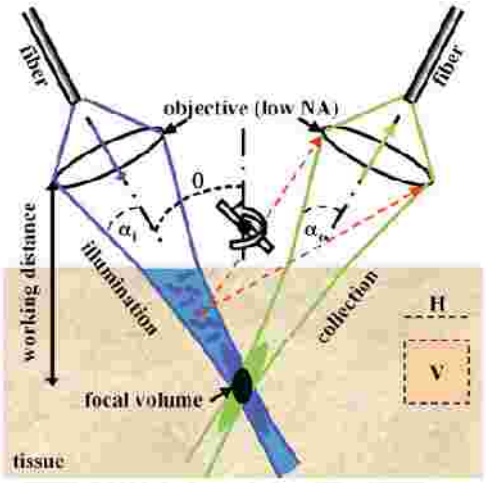

Figure 7 Light schematic of DAC architecture in (Chu *et al.*, 2010).

The results for transverse and axial resolution with Gaussian beam can be calculated by the following equations (Liu *et al.*, 2010):

$$\Delta x_d = \frac{0.466\lambda}{NA(\pi/2\gamma\cos\theta)};\ \Delta y_d = \frac{0.466\lambda}{NA(\pi/2)};\ \Delta z_d = \frac{0.466\lambda}{NA(\pi/2\gamma\sin\theta)} \qquad (2)$$

where NA = n sin a ~ na for low NA objective lens. The DAC architecture, the axial resolution is proportional to 1/NA, rather than 1/ NA^2 in SAC.

2. Designing of MEMS Based Confocal Microscope

A miniature MEMS based SAC microscope which is demonstrated in (Dickensheets and Kino, 1998) use an optical fiber as the illumination and detection pinhole. Their imaging probe is fabricated on a single crystalline silicon substrate embedded two single axis MEMS scanners. (Aguirre *et al.*, 2005; Kumar *et al.*, 2006; Jung *et al.*, 2008; Xie, 2009) present some of MEMS based SAC microscope probe designs, shown in Figure 8, which integrate a MEMS scanner and lenses in miniature package and also demonstrate acquiring system, the end of their reports show result of their applications.

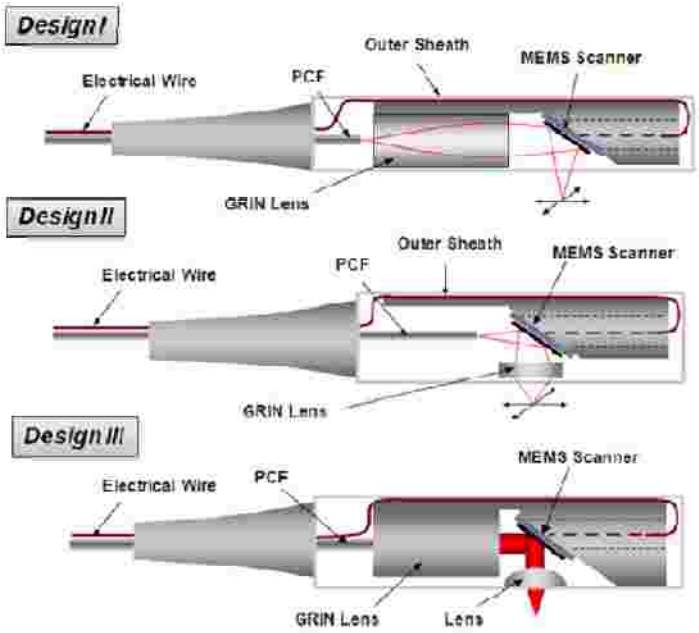

Figure 8 Various designs of MEMS based SAC microscope probe in (Jung *et al.*, 2008).

A single fiber confocal microscope with post-fiber beam scanning by a 2D MEMS scanner with high resolution was demonstrated by (Maitland *et al.*, 2006; Shin *et al.*, 2007). They achieved image acquisition at 8 frames per second with field of view of 140 µm × 100 µm and 0.32 NA. Their schematic diagram of the system shown in Figure 9. A fiber-coupled laser diode with center wavelength of 635 nm is aligned for transmission through a polarizing beamsplitter (PBS1). light is coupled into a single-mode fiber for delivery to deflect at MEMS scanner. At the distal end of this secondary fiber, light passes through a quarter-wave plate (QWP) with its optical axis at 45°. The beam is raster scanned by the MEMS scanner before sent through miniature objective lens and focused on the sample. Backscattering light from the sample is collected to the same miniature objective lens and coupled back into the same single-mode optical fiber. The QWP shifts the polarization of backscattered light through 90º relative to the incident light. On its return to PBS1, only light that has made a round-trip through the QWP will be reflected towards the detector. A second polarizing beamsplitter (PBS2) oriented at 90° to PBS1 is used to

further reduce the amplitude of unwanted reflections reaching a multimode fiber which is connected to avalanche photodiode (APD).

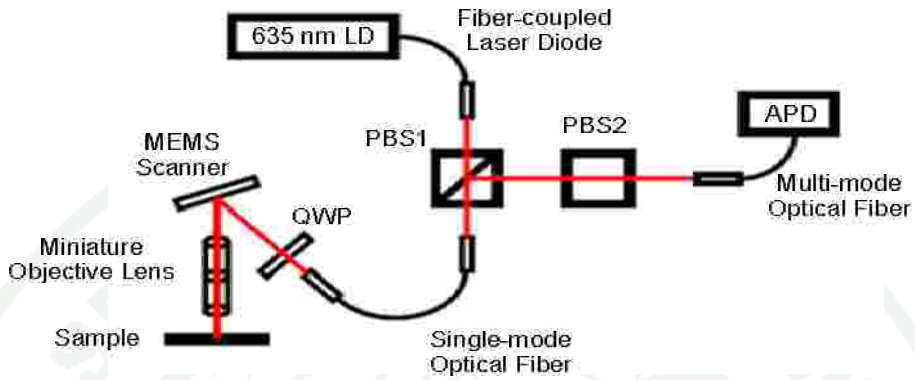

Figure 9 Schematic of single fiber confocal microscope system in (Maitland *et al.*, 2006; Shin *et al.*, 2007).

The optical designs of a 9.6-mm diameter fiber-coupled probe for combining with femtosecond laser microsurgery are analyzed and modeled on optical software program in (Hoy *et al.*, 2011). The optimization reveals that the optical system can be aberration-corrected using simple aspheric relay lenses to achieve diffraction-limited imaging resolution over a large field of view. Moreover, multispectral confocal imaging in (Rouse and Gmitro, 2000) which used multiple wavelengths to acquire an image can extract more biological details.

Furthermore, MEMS scanner can apply to another concept of confocal microscope which is dual axis confocal microscope. (Wang *et al.*, 2003) presented a dual-axes confocal microscope with post objective scanning used low-coherence heterodyne detection to collect vertical cross-sectional images from biological tissue. Then, (Ra *et al.*, 2006; Ra *et al.*, 2007; Piyawattanametha *et al.*, 2009) demonstrate a MEMS based dual axis confocal microscope in a 10-mm-diameter package for three dimensional imaging cooperating with near infrared wavelength. In 2010, MEMS based dual axis confocal microscope incorporating a 1.8-mm-diameter gradient-index relay lens was developed for guidance during resection of brain tumor by (Liu *et al.*, 2010).

By comparing between DAC and SAC architectures, the DAC can archive high axial resolution but it requires more optical alignments and elements while SAC achieves much lower axial resolution but it composes of a simpler architecture and fewer optical elements which are more feasible to miniaturize imaging probe than the DAC configuration.

3. MEMS Scanner's Scanning Scheme

As aforementioned, MEMS scanner is used to steer laser beam over image plane so that MEMS scanner movement will effect to geometry of the image. This section will describe some of MEMS scanner scanning patterns.

3.1 MEMS Based Raster Scanning

Raster scanning is a rectangular scanning pattern. The pattern consists of parallel lines which are arranged in orthogonal direct as in Figure 10. This scanning pattern is a systematic process for covering area progressively or one line at a time.

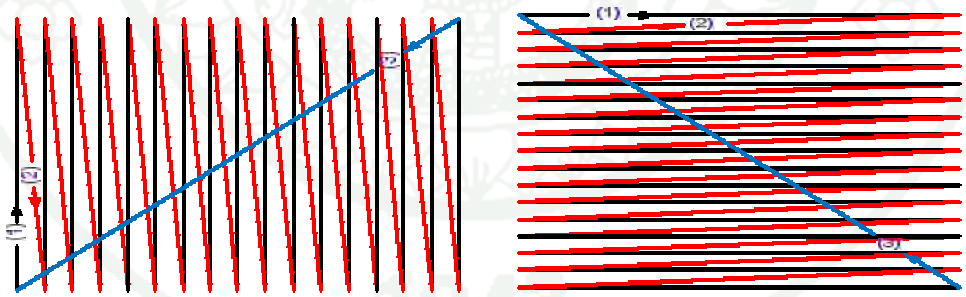

(a) (b)

Figure 10 Raster scanning (a) Vertical (b) Horizontal.

To implement in MEMS based raster scanning, one axis of MEMS scanner is actuated with sinusoidal signal at resonant frequency will cause MEMS scanner moves at maximum angle and another direction is actuated with triangular signal at slow frequency. The moving pattern of laser point on the sample and the example image from (Piyawattanametha *et al.*, 2009) are shown in Figure 11.

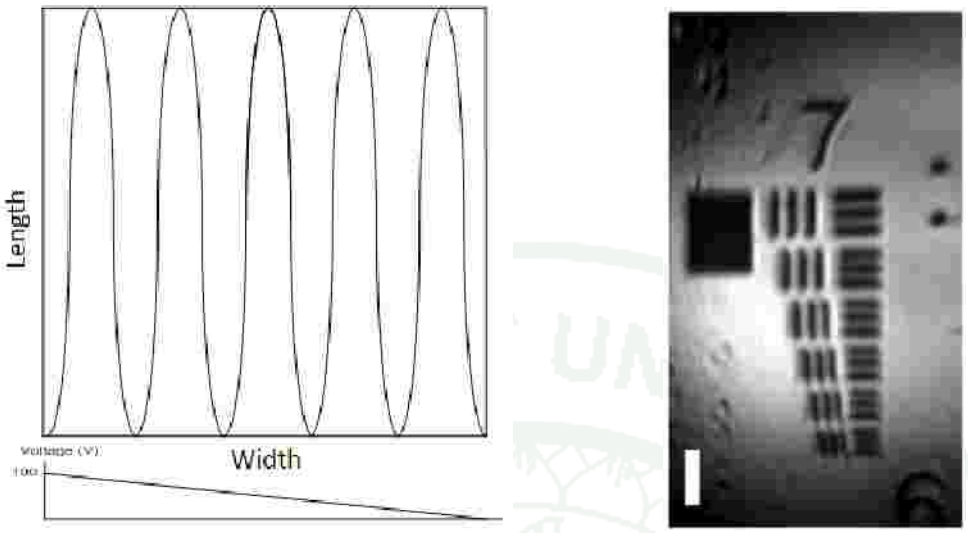

(a) (b)

Figure 11 Image from raster scanning (a) The moving pattern of laser point on the Sample, (b) Example image from (Piyawattanametha *et al.*, 2009).

3.2 MEMS Based Lissajous Scanning

Lissajous scanning pattern is form when two vibrations along perpendicular lines are superimposed. Let each vibration be a simple harmonic motion represented by a sinusoidal wave; let a and b denote the amplitudes, ω_1 and ω_2 the angular frequencies (in radians per second), ϕ_1 and ϕ_2 the phases and t the time.

$$x = a\ \sin(\omega_1 t + \phi_1), \quad y = b\ \sin(\omega_2 t + \phi_2) \tag{3}$$

One other observation is worth mentioning. As long as frequency ratio ω_1 / ω_2 is a rational number, the curve will eventually repeat itself, causing the motion to be periodic. But if ω_1 / ω_2 is irrational, the path will be never retraced, resulting in a non-periodic motion. However, as time progresses the curve will gradually fill the rectangle bounded by the line $x = \pm a$, $y = \pm b$.

The MEMS based Lissajous scanning pattern is created by actuating both axes of MEMS scanner with resonant frequency, mostly ω_1 / ω_2 is irrational, enabling large field of view image. MEMS based unstable Lissajous scanning pattern is achi by

(J. T. C. Liu *et al.*, 2010). Their resulting scanning pattern is described by the following parametric equation as a function of time:

$$x = A\ \sin(2\pi at + \phi_x) + A \tag{4}$$

$$y = B\ \sin(2\pi bt + \phi_y) + B \tag{5}$$

where ϕ_x and ϕ_y are phase shift constants (in radian), a and b are the slow and fast frequencies, respectively.

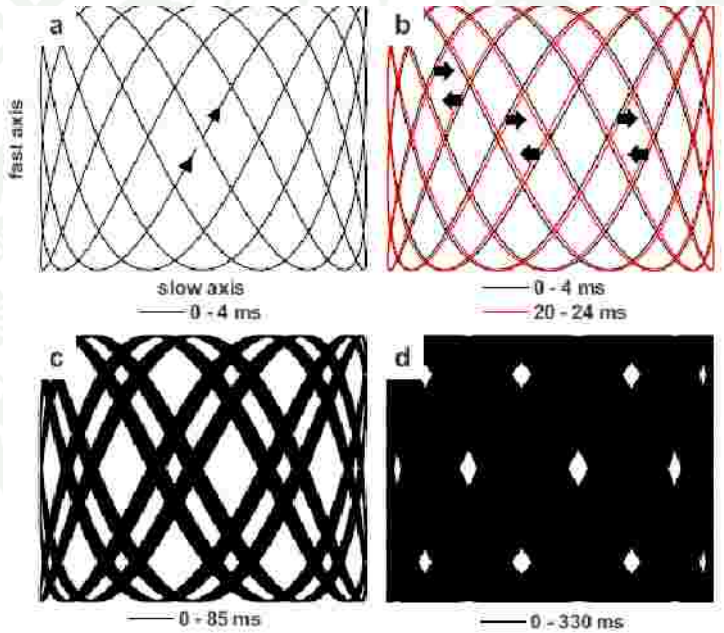

Figure 12 Calculated Lissajous scan patterns in (Liu *et al.*, 2010). Fast-axis frequency=2219 Hz. Slow-axis frequency=986 Hz, (a) 0 to 4 ms, (b) A comparison of two Lissajous patterns20 ms apart, showing how the pattern shifts over time, (c) 0 to 85 ms, showing partial coverage over the field of view, (d) 0 to 330 ms, showing nearly full coverage over the field of view.

3.3 MEMS Based Vector Scanning

Vector scanning operates by tracing only the path required to acquire the image while raster scanning must acquire the entire field of view. Vector scanning requires significantly less memory; do not suffer from aliasing and pixilation effects.

(Milanovic, 2007) demonstrated MEMS based vector scanning with low pass filter for smoothing transition. Their raw path data consist of a list of points for each frame then they are filtered depending on the type of filter that is chosen. The simplest filtering scheme applies a digital Butterworth or Bessel low pass filter while the feed forward filter uses information about the device resonant frequency and Q to compute a nearly optimal input waveform given the system bandwidth limitations (Castelino *et al.*, 2005; Milanovic, 2007). In below figure shows the method to input signal to MEMS scanner in vector scanning which is demonstrated (Milanovic, 2007). Because deflect angle of MEMS scanner depend on square term of supply voltage so the desired position stream is squared root then it is send through low pass filter for smoothing movement before supply signal to MEMS scanner.

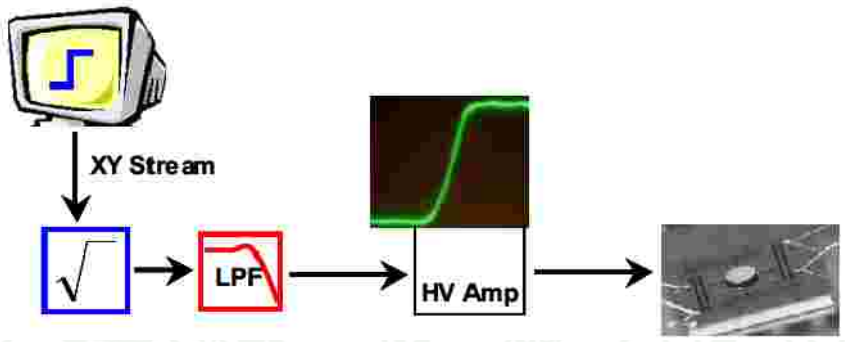

Figure 13 Schematic of MEMS based vector scanning system in (Milanovic, 2007).

4. Linearization Approaches

The electrostatically actuated 2D MEMS scanner has a major problem associated with its operation which is nonlinearity movement. This section will present the detail of literature review of linearization approached.

4.1 Differential Driving Scheme

Applying a small control voltage over a large bias voltage is a well-know technique to improve the linearity of limited ranges for parallel plate electrostatic actuator, whose output is governed by square of voltage (Toshiyoshi *et al.*, 2001). However, the differential driving scheme performs best on the occasion that the capacitance derivative with respect to the rotation angle $\partial C/\partial \theta$ remains constant but vertical comb drive actuators, which $\partial C/\partial \theta$ can be considered quasi-constant. Due to the fact that, at the side that travels upward during rotation, the movable comb parts away from the fixed comb and their overlap vanish as Figure 14. Therefore, the opposite torque fails to be established (Tsai *et al.*, 2008).

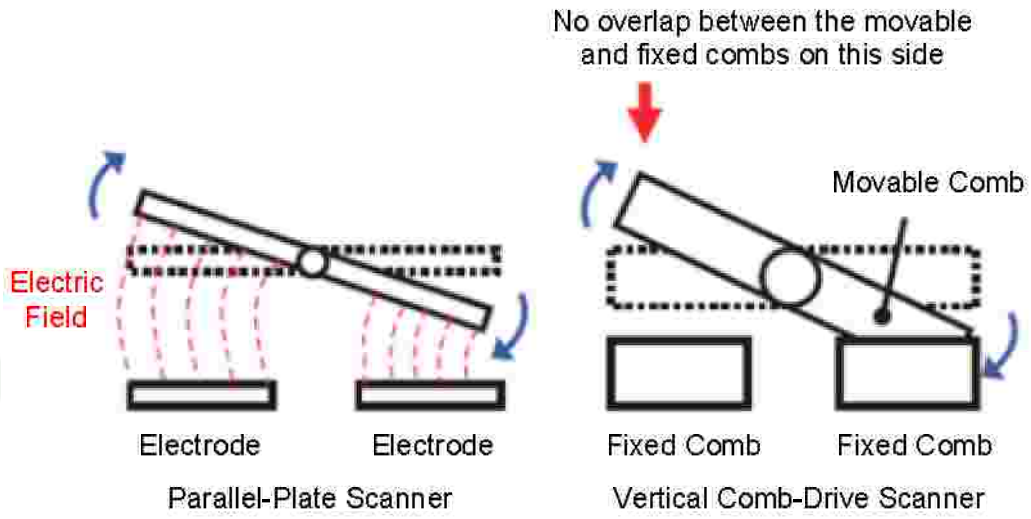

Figure 14 Comparison between parallel-plate and vertical comb-drive actuators.

(Poland *et al.*, 2009; Milanovic, 2009; Chao *et al.*, 2011) utilize a new method to drive MEMS scanner with differential the bias voltage in order to linear devices and to provide smooth transitions. Therefore, they can actually create a push-pull situation with both opposing comb drives. The push-pull situation can create torque at any point in their rotation, shown in Figure 15. This results nearly linear voltage vs. angle mirror characteristics for all such devices.

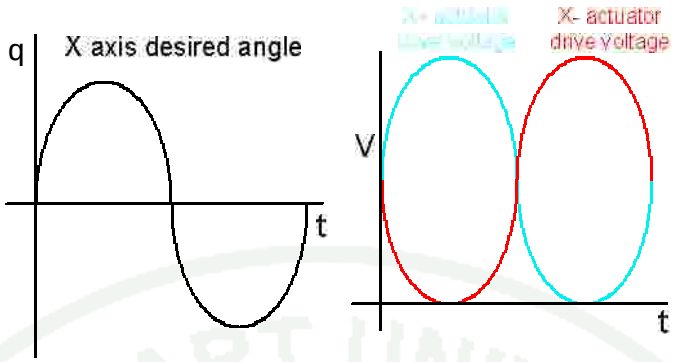

Figure 15 Methodology of differential the bias voltage.

4.2 Neural Network Scheme

The neural network (NN) is suitable for nonlinear function approximation. Neural network can be created by supplying the pairs of input and output samples and determining the proper training rules. The neural network is able to generate the correct output based on the derived neural nodes. (Zhou *et al.*, 2003) proposed a bayesian regularization based neural networks approach. A Bayesian regularization back-propagation is a network trained by updating the weight and bias values according to Levenberg-Marquard optimization. A feedforward neural network is used to control an electrostatically actuated optical switch in (Aribe and, 2005).The strength of neural computing approach lies in its abil to learn and adapt to changes in the variant environmental conditions.

(Zhao *et al.*, 2005) reported a radial basis function (RBF) neural network method to linearize the scanning field of a 2D MEMS scanner with parallel plate structure, which is distorted by the intrinsic nonlinearity of the electrostatic torques. The idea of linearizing the scanning field by RBF neural network is illustrated in Figure 16. The input pair (V_{ix}, V_{iy}) is mapped to the expected positions of spot ($\hat{x}_{PSD}, \hat{y}_{PSD}$) on photo-sensing-detector (PSD) linearly. The expected positions output is then fed to the RBF neural network to produce the actual voltage pair (V_x, V_y)

required to drive the 2D MEMS scanner to the actual positions (x_{PSD}, y_{PSD}). They define the MEMS scanner system as the following mapping:

$$f(g):\begin{pmatrix} V_x \\ V_y \end{pmatrix} \rightarrow \begin{pmatrix} x_{PSD} \\ y_{PSD} \end{pmatrix} \tag{6}$$

The inverse of the above mapping is

$$\dot{f}^{-1}(g):\begin{pmatrix} x_{PSD} \\ y_{PSD} \end{pmatrix} \rightarrow \begin{pmatrix} V_x \\ V_y \end{pmatrix} \tag{7}$$

The RBF neural netwok is designed to approximate the inverse mapping. But there always exists some approximation error, the actual mapping of the RBF neural network is $\dot{f}^{-1}$.

$$\dot{f}^{-1} g f = I + \Delta \tag{8}$$

where ? is the approximation error matrix. The position of the laser spot on the PSD is expressed by the following equation:

$$\begin{pmatrix} x_{PSD} \\ y_{PSD} \end{pmatrix} = \begin{pmatrix} V_{ix} \\ V_{iy} \end{pmatrix} \begin{pmatrix} k_x & 0 \\ 0 & k_y \end{pmatrix} (I + \Delta) \tag{9}$$

where k_x, k_y are scale parameters specified by the user.

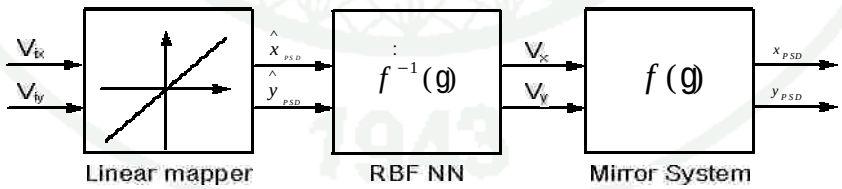

Figure 16 Scheme of the linearization by RBF NN in (Zhao, Tay et al. 2005).

MATERIALS AND METHODS

Materials

1. Personal Computer
2. MATLAB Simulation software
3. Microsoft Excel software
4. Mathcad software
5. Zemax software

Methods

Due to MEMS based single axis confocal microscope consists of two important components which are MEMS scanner and confocal probe so, this chapter will presents design concept and theoretical analysis single axis confocal microscope probe and MEMS scanner control. In design methodology, the performance of single axis confocal microscope probe is improved by eliminating the chromatic aberration of lens system. Moreover, the image of MEMS based single axis confocal microscope use point-by-point scanning scheme in imaging process so that MEMS scanner has to steer laser beam over the sample. ntly, MEMS scanner control methodology also has to be considered d improved. In this thesis, linearization with RBF neural network for MEMS scanner for MEMS based single axis confocal microscope is developed. In addition, the design and performance analysis of a miniature single axis confocal microscope probe for multiple wavelengths is presented in section 1. Furthermore, MEMS scanner's characteristic simulation for neural network's training process and the development of linearization with RBF neural network to control MEMS scanner for MEMS based single axis confocal microscope are presented in section 2 and section 3, respectively.

1. Miniature Single Axis Confocal Microscope Probe for Multiple Wavelengths

Principle of MEMS based single axis confocal microscope (Dickensheets and Kino 1996; Kumar *et al.*, 2006; Maitland *et al.*, 2006; Chantakien *et al.*, 2011) is illustrated in Figure 17. An optical fiber is used for illumination and detection pinhole to reject out of focus light. The laser light laser source is coupled to a single mode optical fiber before it is split into two fibers with 50:50 power ratios by an optical fiber coupler. At one end of fiber coupler, the exiting light from optical fiber is collimated while at another end, an optical fiber is terminated. Figure 17 shows a miniature single axis confocal probe (Maitland *et al.*, 2006) which consists of two parts. Those are a beam expander referred to Keplerian telescope configuration and an objective lens. A 2D MEMS scanner steers an input illumination over the first surface of a Keplerian telescope. As a a focused spot is scanned across over an image plane. The 2D MEMS scanner is actuated to scan in 2D by using high electrical voltage signals. The high electrical voltage signals are generated from data acquisition system before they are amplified by high voltage amplifier. In order to increase a laser beam diameter, the Keplerian telescope is applied to expand the laser beam after scanning by a 2D MEMS scanner while telecentricity is maintained. Finally, the laser beam is focused to a small spot at image plane by an objective lens.

Backscattering light from the image plane is collected by the same objective lens and Keplerian telescope before it is coupled back into the same optical path. On the data acquisition system, a 2D image is created by electrical input signal that is converted from light intensity by a photo detector. In order to map electrical input signal with each scanning position, time synchronization between driving signals and electrical input signal is performed.

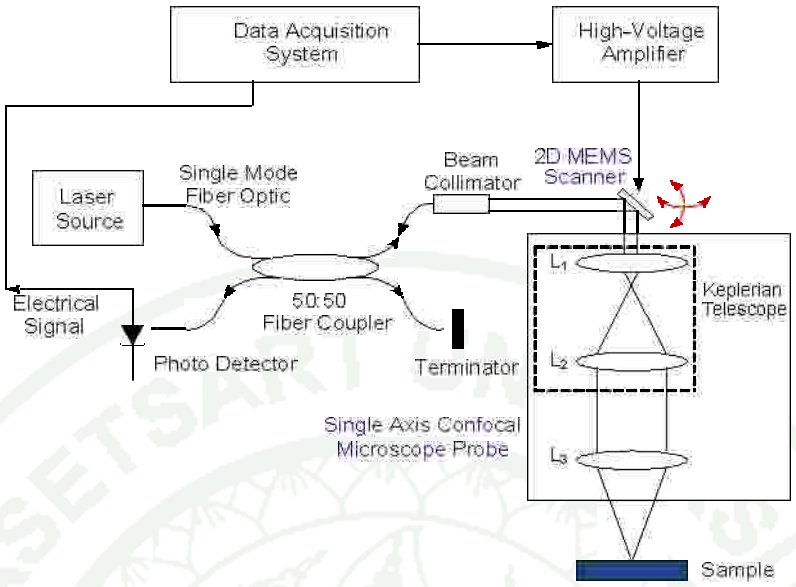

Figure 17 Configuration of MEMS based single axis confocal microscope.

As aforementioned, a Keplerian telescope is used to increase the diameter of a collimated laser beam. A Keplerian telescope consists of two positive lenses that are separated by the sum of their focal lengths, shown in Figure 18.

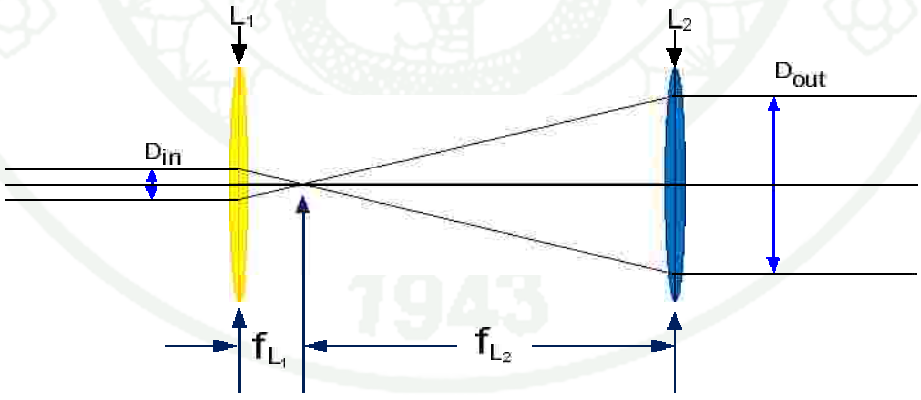

(a)

Figure 18 Configuration of Keplerian telescope (a) Magnifying power of Keplerian Telescope, (b) Ray tracing of off axis laser beam.

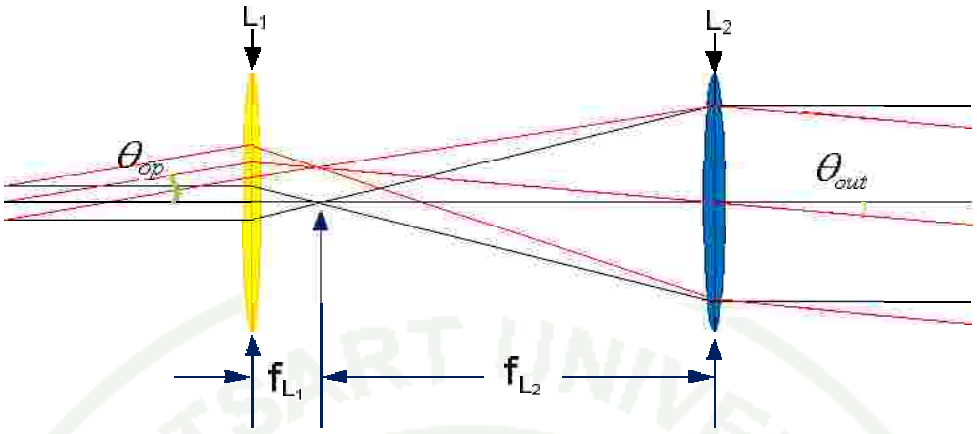

(b)

Figure 18 (Continued).

The magnifying power and minifying angle of Keplerian are based on their focal lengths. Thus, equations are as following;

$$\text{Magnifying Power} = \frac{D_{out}}{D_{in}} = \frac{f_{L_2}}{f_{L_1}} \tag{10}$$

$$\text{Minifying Angle} = \frac{\theta_{out}}{\theta_{op}} = \frac{f_{L_1}}{f_{L_2}} \tag{11}$$

After Keplerian telescope, the laser beam will approach an objective lens in an angle (θ_{out}) as a result of the laser beam that is focused about spot at $f_{L_3}\theta_{out}$ on image plane, as shown in Figure 19. Consequently, the of a spot on image plane relates to deflected angle of light (θ_{op}) with linear function.

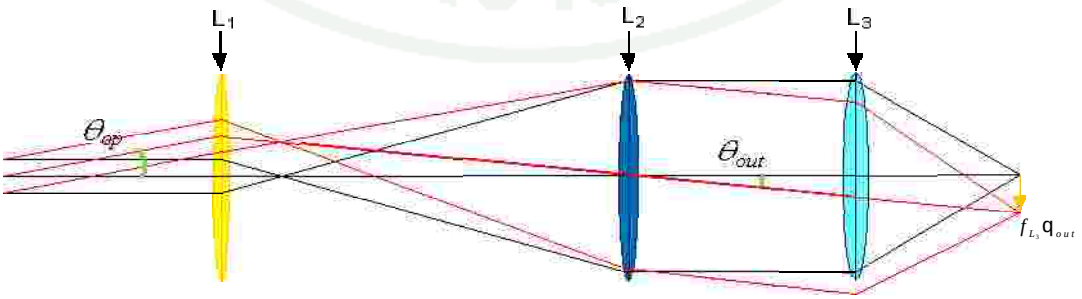

Figure 19 Focusing the off-axis laser beam on the image plane.

An essential problem of miniature single axis confocal microscope probe for multiple wavelengths is chromatic aberration. It is the failure of lens to focus all wavelengths to the same convergence point, as shown in Figure 20(a), because lens's material has different refractive index for different velengths. Fortunately, achromatic lens is designed to reduce the effects of chromatic aberration by "bringing" the focal point of two wavelengths (typical red and blue) to the same point. The most achromatic lenses compose of two individual lens's materials which are made from glasses with different amounts of dispersion, shown in Figure 20(b). Therefore, a miniature single axis confocal microscope probe for multiple wavelengths can be designed with achromatic lenses to the effect of chromatic aberration.

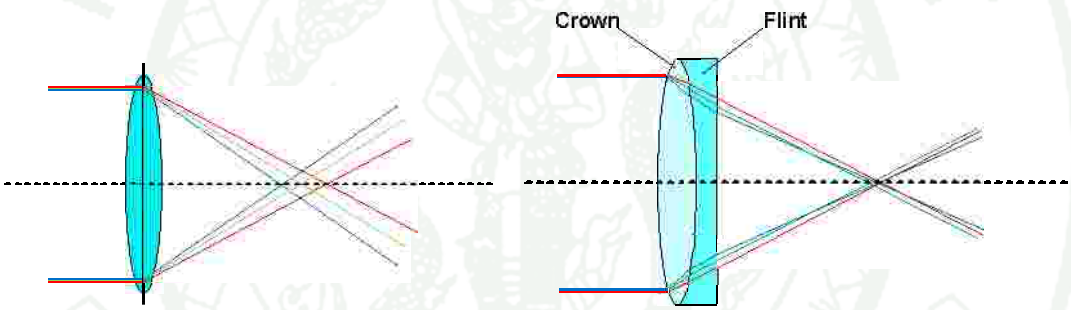

Picture from http://en.wikipedia.org/wiki/Achromatic_lens

Figure 20 Property of Achromatic doublet lens (a) chromatic aberration, (b) achromatic doublet lens.

Schematic of a miniature single axis confocal microscope probe for multiple wavelengths from (Chantakien *et al.*, 2011) is depicted in Figure 21. This schematic present the simulation of optical ray tracing after the MEMS mirror reflected off the incoming laser beam. The 2D MEMS scanner reflects the laser beam at 0º, 4º, and 8º (along y-axis), as shown in Figure 21. Each color represents deflection angle (blue for zero degree, green for four degrees, and red for eight degrees). Two 3 mm diameter achromatic lenses with focal length of 4.5 mm and 12 mm (TECHSPEC Company) are used to expand the beam size from 0.5 mm to 1.3 mm, respectively. An achromatic lens, focal length 2 mm (TECHSPEC Company), is as an

objective lens to focus laser beam to image plane. The total distance between 2D MEMS scanner to image plane is 39.61 mm. The system is 0.21 NA.

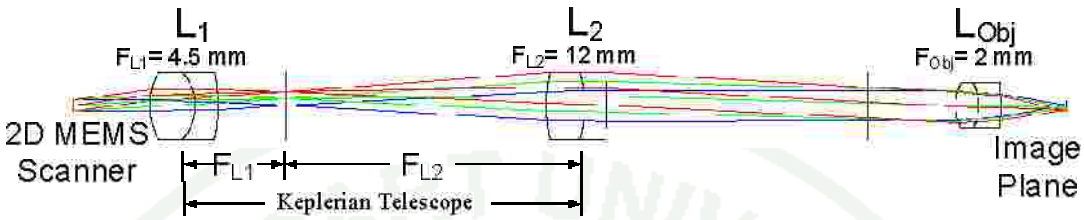

Figure 21 Schematic of a miniature single axis confocal microscope probe for multiple wavelengths.

Consequently, the spot diagram indicating in Figure 22 shows geometry of each ray tracing on image plane. Because diffraction limit is the ability to produce image with acceptable angular resolution for an optical system, the spot diagram indicates the ability of the system to achieve diffraction limit by showing the region of Airy disc. The Airy disc of this configuration, solid-line circle, is 3.428 µm diameters.

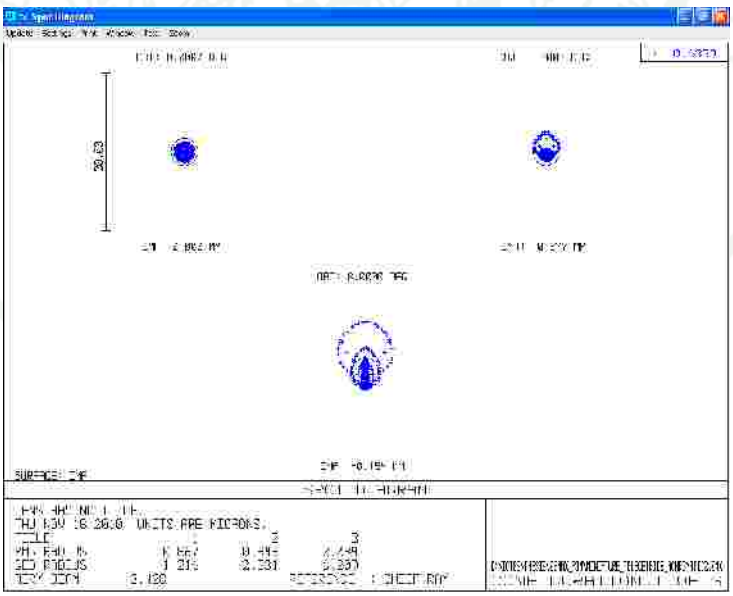

Figure 22 Spot diagram.

Furthermore, we simulate the ability our imaging system to transfer contrast from the object at particular resolution level by using modulation transfer function (MTF) which is the relative modulus of the optical transfer function (OTF). The MTF for tangential (T) and sagittal (S) responses of each deflected angle is shown in Figure 23. Diffraction limit MTF is shown with a solid line. system performance is predicted via this MTF plot with the largest deviation of the maximum angle. The smallest spatial frequency value achieves when MEMS scanner deflects the light at eight degrees. Therefore, both T and S responses decrease to a half of their maximum value at spatial frequency 130.14 cycles per millimeter (7.68 µm per cycle or 55.04% from diffraction limit) and 258.04 cycles per millimeter (3.87 µm per cycle or 10.86% from diffraction limit), respectively. Corresponding to cut off (0% contrast), their spatial frequency is derived at approximately 680 cycl per millimeter (1.47 µm per cycle same as diffraction limit) which is the same as at the diffraction limit.

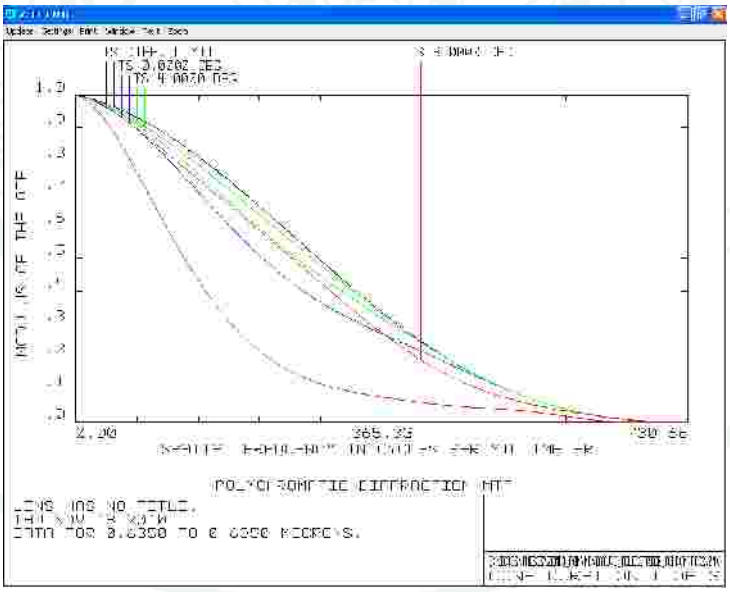

Figure 23 MTF graph.

The chromatic axial focal shift graph covering wavelength from 488 nm to 785 nm, Figure 24, indicates that the focal point shift inward of 2.56 µm for 488 nm wavelength, and shift outward of 5.96 µm for 785 nm wavelength, centering at 635 nm wavelength.

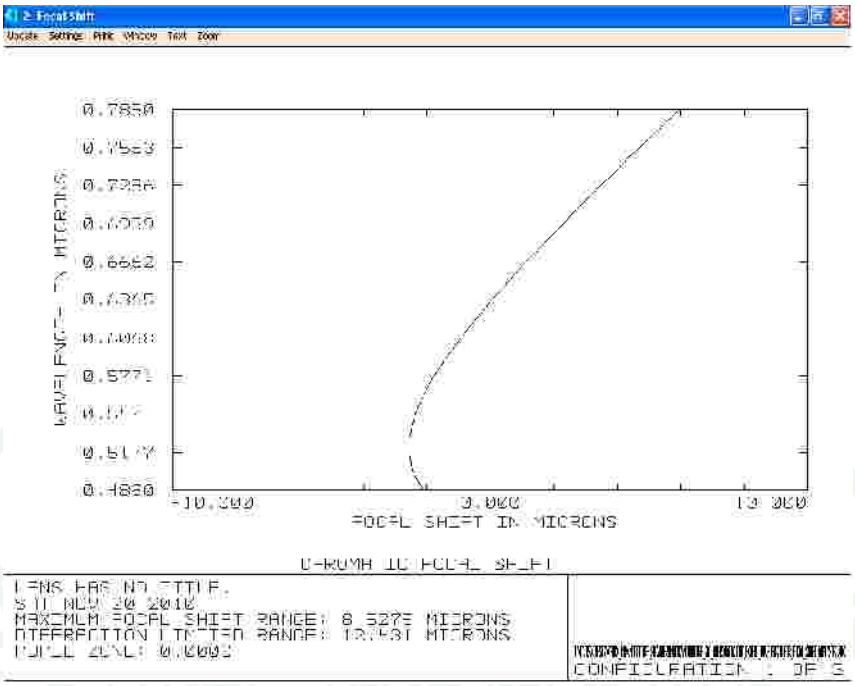

Figure 24 Focal shift graph.

As aforementioned, the spot positions on image plane relate to light deflected angle with linear function. Therefore, the miniature s le axis confocal microscope probe for multiple wavelengths is characterized via ZEMAX program to find the relationship between spot positions on image plane and light deflected angle. The result can be written in (12) and Figure 25. The minus sign indicates the direction of spot is opposite to the light deflected angle.

$$d = -19\ \theta_{op} \quad \mu m. \qquad (12)$$

where d is displacement distance measured from center and θ_{op} is light deflected angle.

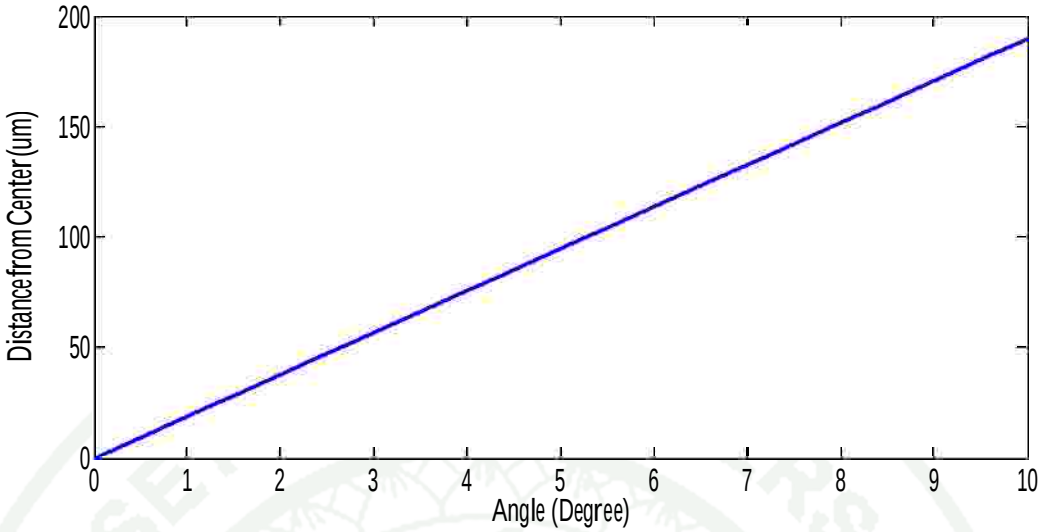

Figure 25 Displacement distance from center versus light deflected angle.

2. D MEMS Scanner Characteristic Simulation

The characteristic simulation in this thesis refers to MEMS scanner's model and calculation in (Piyawattanametha *et al.*, 2005). The schematic of the 2D AVC MEMS scanner in (Piyawattanametha *et al.*, 2005) is shown in Figure 26. The inner mirror can be actuated to rotate around the inner torsion beam while the outer frame can be actuated to rotate around the outer torsion bea Therefore, the inner mirror and outer frame can orthogonally rotate with respect to each other. This 2D AVC MEMS scanner has 16 comb bank divided into 8 of movable comb banks with 10 fingers and 8 fixed comb banks with 11 comb fingers. The overall dimension of the scanner is 2.7 mm x 2.9 mm. The other parameters of this scanner are shown in Table 1.

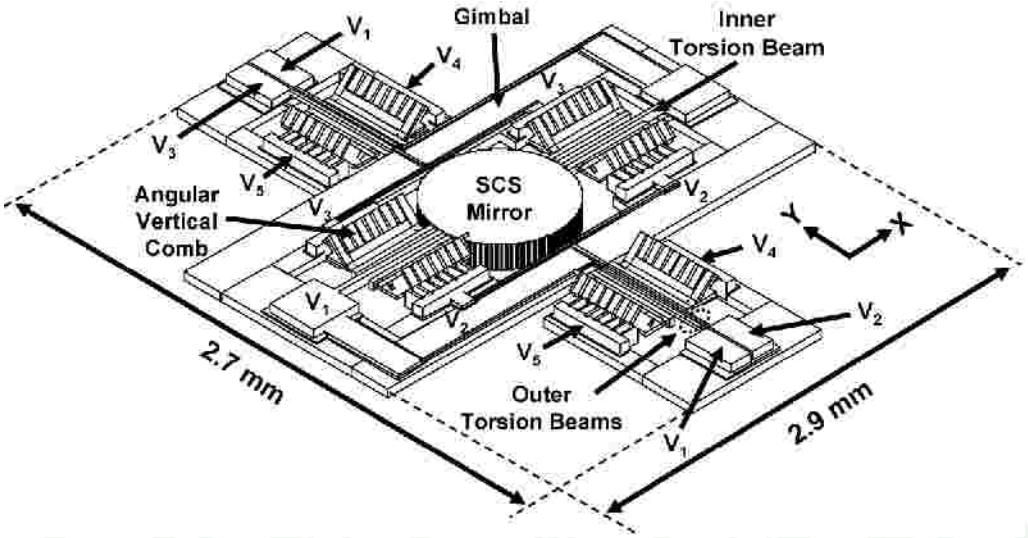

Figure 26 Schematic of the 2D AVC scanner in (Piyawattanametha *et al.*, 2005).

Table 1 Parameters of 2D MEMS scanner in (Piyawattanametha *et al.*, 2005)

Parameter	Expression	Nominal Values
Mirror and comb finger thickness	T_m, T_f	35 µm
Inner torsion beam width	w_{si}	10 µm
Inner/Outer torsion beam length	l_{si},l_{so}	345 µm
Outer torsion beam width	w_{so}	12 µm
Inner/Outer torsion beam thickness	t_s	3.5 µm
Initial angle	$?_i$	10 degree
Comb finger size	w_f	4.6 µm
Comb finger Length	L_f	242 µm
Comb finger gap spacing	g_f	4.4 µm
Movable comb finger clearance	L_{fo}	135 µm
Movable comb finger offset	L_{co}	35 µm
Number of movable comb fingers	N_{finger}	20

An electrostatic torque, $T_e(?,V)$, effects to movable comb fingers when an electrical voltage is applied to fixed comb fingers while movable comb fingers is connected to ground. The difference voltage level between fixed comb fingers and movable comb fingers creates electrostatic force attaching down movable comb

fingers as a result the overlapping area between fixed comb fingers and movable comb fingers increase upon applied electrical voltage. The mechanical restoring toque, $T_r(?)$, is created by torsion beam to resist rotation of movable comb fingers. At equilibrium angle, electrostatic torque and mechanical restoring toque will equal.

$$T_e(\theta, V) = NV^2 \frac{\partial C_{unit}(\theta)}{\partial(\theta)} \tag{13}$$

$$T_r(\theta) = \frac{2Gw_s^3 t_s}{3l_s}\left[1 - \frac{192}{\pi^5}\frac{w_s}{t_s}\tanh\left(\frac{\pi}{2}\frac{t_s}{w_s}\right)\right]\theta \tag{14}$$

At equilibrium angle:

$$T_e(\theta, V) = T_r(\theta) \tag{15}$$

$$NV^2 \frac{\partial C_{unit}(\theta)}{\partial(\theta)} = \frac{2Gw_s^3 t_s}{3l_s}\left[1 - \frac{192}{\pi^5}\frac{w_s}{t_s}\tanh\left(\frac{\pi}{2}\frac{t_s}{w_s}\right)\right]\theta \tag{16}$$

The $C_{unit}(?)$ is capacitance between a movable comb finger and a fixed comb finger at ? degree. To archive $C_{unit}(?)$, the capacitance of a movable comb finger and a fixed comb finger at any offset height, $C_{unit}(z)$, is estimated by using 2-D finite element program (using FEMLAB from COMSOL, Inc.). (Hah 2004; Piyawattanametha 2005) present the calculation of fringe fields between two comb fingers. The result of $C_{unit}(z)$ is a function related to finger offset height, shown in Figure 27. The inset shows the cross section of a movable comb finger (denoted ***M***) and a fixed comb (denoted ***F***) fingers.

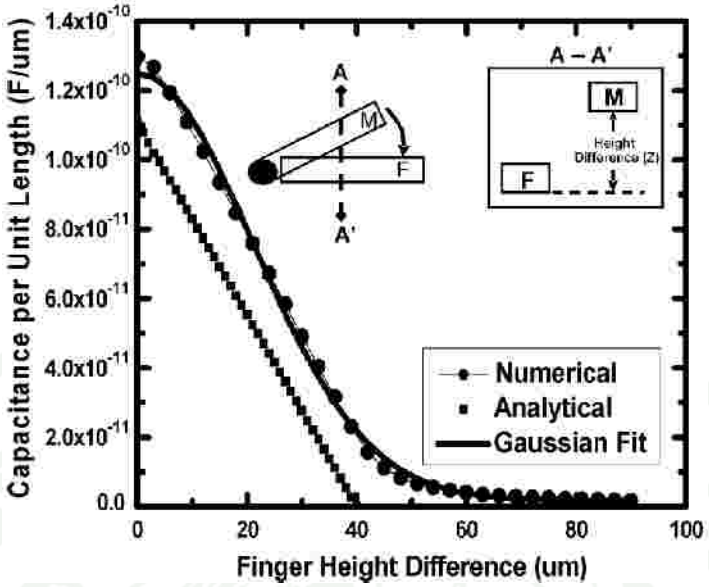

Figure 27 The capacitance per unit length versus the finger offset in (Piyawattanametha *et al.*, 2005).

These numerical calculation of $C_{unit}(z)$ in (Piyawattanametha *et al.*, 2005) is fitted to be a Gaussian curve by applying parameters C_1,C_2, and C_3 to the following equation.

$$C_{unit}(z) = C_1 + C_2 \exp(-C_3 z^2) \qquad (17)$$

Therefore, unit capacitance, $C_{unit}(?)$, will be estimated analytically by $C_{unit}(z)$ of overlapping area along movable comb finger length. integration of $C_{unit}(z)$ needs to take into account of the offset that varies with position in *x* direction and rotating angle *(?)* as Figure 28.

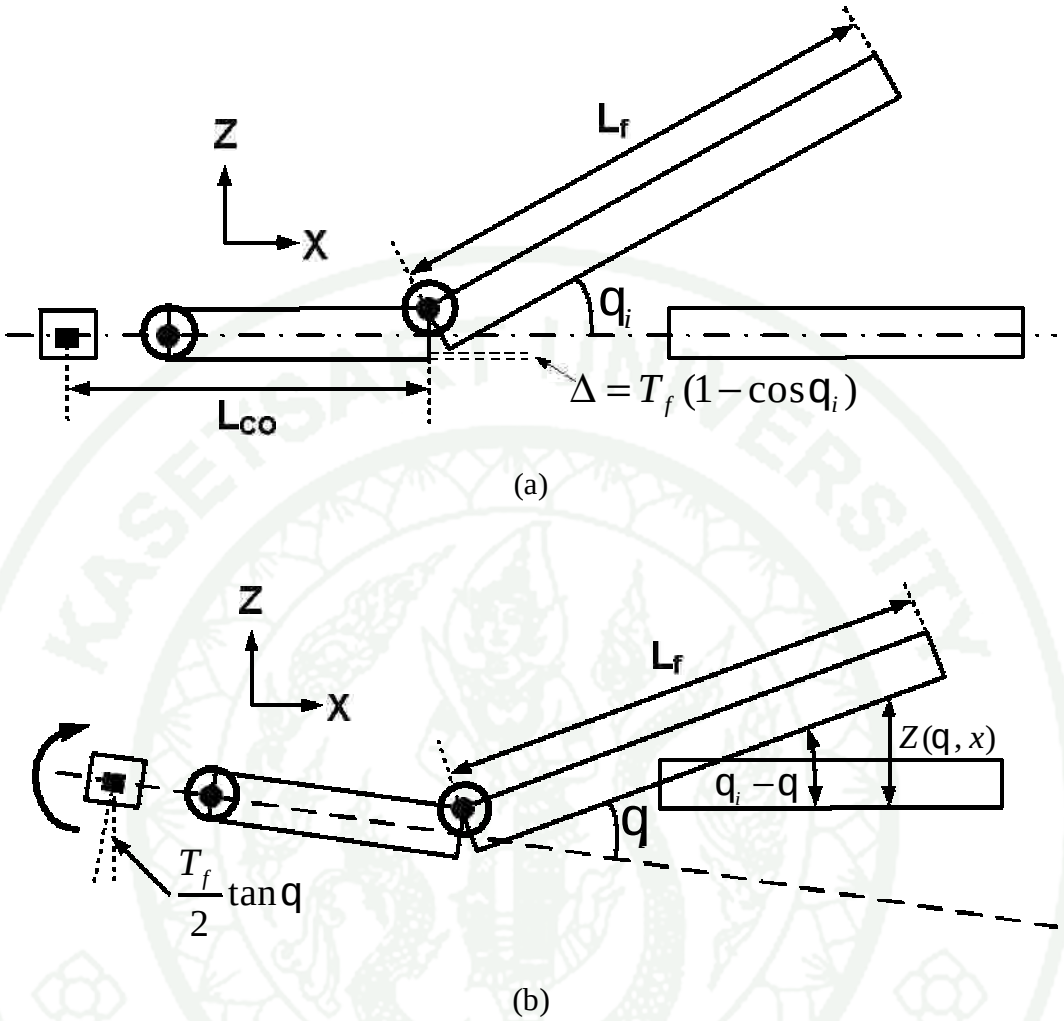

Figure 28 Movable comb finger in (W. Piyawattanametha *et al.*, 2005) (a) initial Stage, (b) under actuation.

The vertical distance, *z* variable which is measured from bottom edge of fixed comb finger to bottom edge of movable comb finger, is function of the rotating angle, *?*, and position on x axis, *x*, as (18).

$$Z(\theta, x) = x\sin(\theta_i - \theta) - \left[L_{co} - \frac{T_f}{2}\tan(\theta) \right]\sin(\theta) + T_f(1-\cos\theta_i) \tag{18}$$

Therefore, $C_{unit}(?)$ can be calculated by a finite integral on (19):

$$C_{unit}(\theta) = \int_{\frac{L_{fo}}{\cos(\theta_i - \theta)}}^{L_f} C_{unit}(Z(\theta, x))dx \tag{19}$$

According to $C_{unit}(?)$ and parameter in Table. 1, the equilibrium angle of applied DC voltage can be archived by (16). To create istic graph the equilibrium angles for given bias voltages on each electrode need to be calculated on Mathcad program. However, the whole model of MEMS scanner cannot be calculated at the same time.

Equilibrium angle calculation will be split into inner mirror (V_2 and V_3) and outer frame (V_4 and V_5) because V_2's structure same as V_3's structure, inner mirror, and V_4's structure same as V_5's structure, outer frame. Each of electrode pairs can move on one major axis only (either X axis or Y axis). Therefore, the characteristic graph between equilibrium angle and applied direct current (DC) voltage of inner mirror and outer frame can be created in Figure 29. The corresponding equilibrium angles are calculated by determining input voltage starts from 0V to 150V, stepping 0.25 V.

MEMS scanner is deployed for light deflection. The position of spot on image plane depends on DC electrical voltage and the selection of actuation electrodes. However, the moving direction of spot on image plane is opposite to MEMS scanner rotation due to lens's property. Furthermore, the light's schematic of a 2D MEMS scanner, a miniature confocal microscope probe, and image plane can be presented in Figure 30. Each of actuation electrodes corresponds to spot movement, V_2 actuation will move spot on X+ axis, V_3 will move spot on X- axis, V_4 will move spot on Y- axis, and V_5 will move spot on Y+ axis.

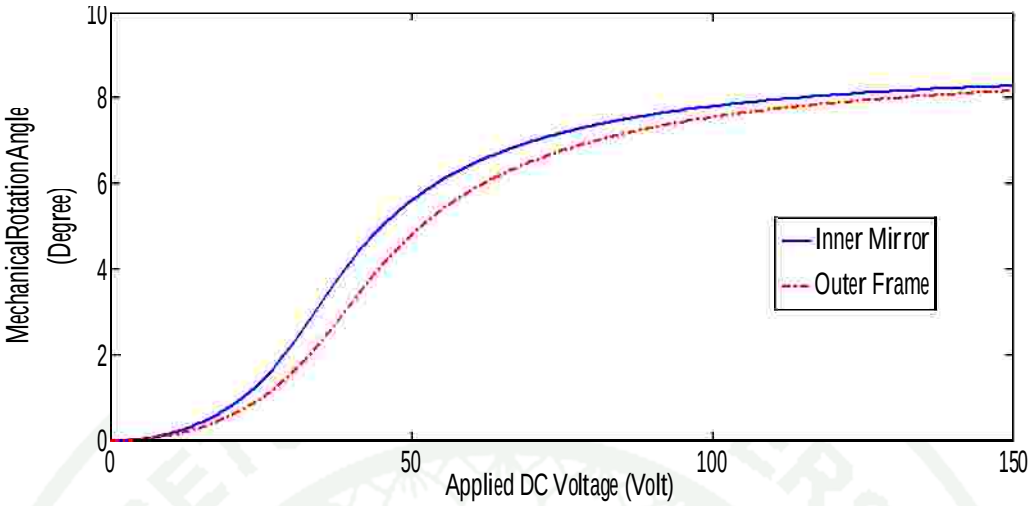

Figure 29 DC scanning characteristic of a 2D AVC MEMS scanner in (Piyawattanametha *et al.*, 2005).

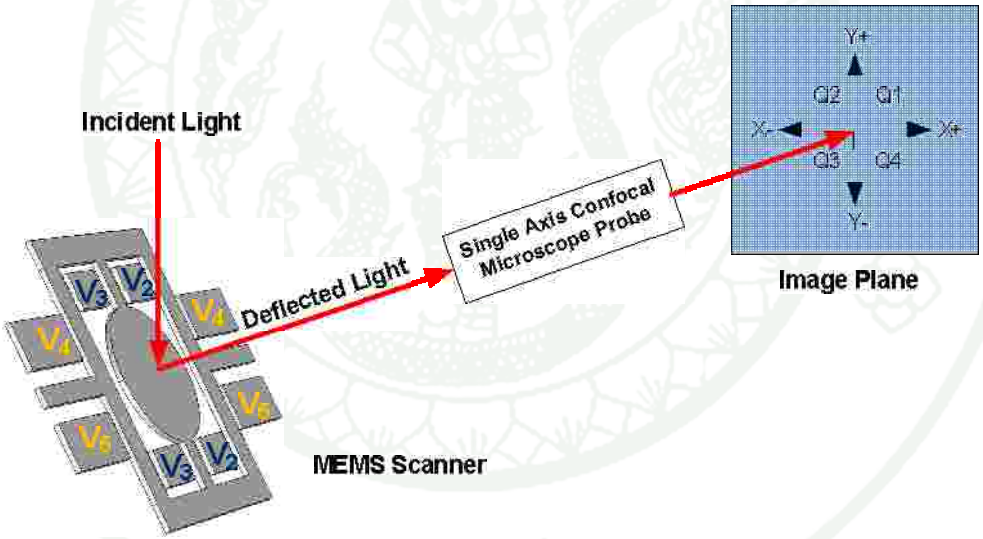

Figure 30 Light's schematic and image plane.

Consequently, the position of spot on image plane can predicted by controlling voltage on selected actuation electrodes as Table 2.

Table 2 Relationship of actuation voltage and the position of spot on the image plane.

Quadrant	Actuation Voltage
Q1	V_2 , V_5
Q2	V_3 , V_5
Q3	V_3 , V_4
Q4	V_2 , V_4

2.1 Light Reflection of MEMS Scanner

In section 1, the displacement of spot on image plane to light deflected angle (θ_{op}) is shown in (12). The relationship between the incident light and deflected light due to MEMS scanner rotation can use law of light reflection in vector form which is derived in (Toshiyoshi *et al.*, 2001).

$$r = i - 2(i \cdot m)m \tag{20}$$

where $\mathbf{i}$ is vector of incident light, $\mathbf{r}$ is vector of reflect light, and $\mathbf{m}$ is vector of normal vector of 2D MEMS scanner. After tilting angle θ and ϕ , the normal vector of 2D MEMS scanner $\mathbf{m}$ is modified by:

$$\mathbf{m} = \begin{pmatrix} \cos\phi & 0 & \sin\phi \\ \sin\theta\sin\phi & \cos\theta & -\sin\theta\cos\phi \\ -\cos\theta\sin\phi & \sin\theta & \cos\theta\cos\phi \end{pmatrix} \mathbf{m}_0 \tag{21}$$

The optical system and parameters are illustrated in Figure 31. The vectors $\mathbf{i}$, $\mathbf{r}$, and $\mathbf{m}$ are always unit vector.

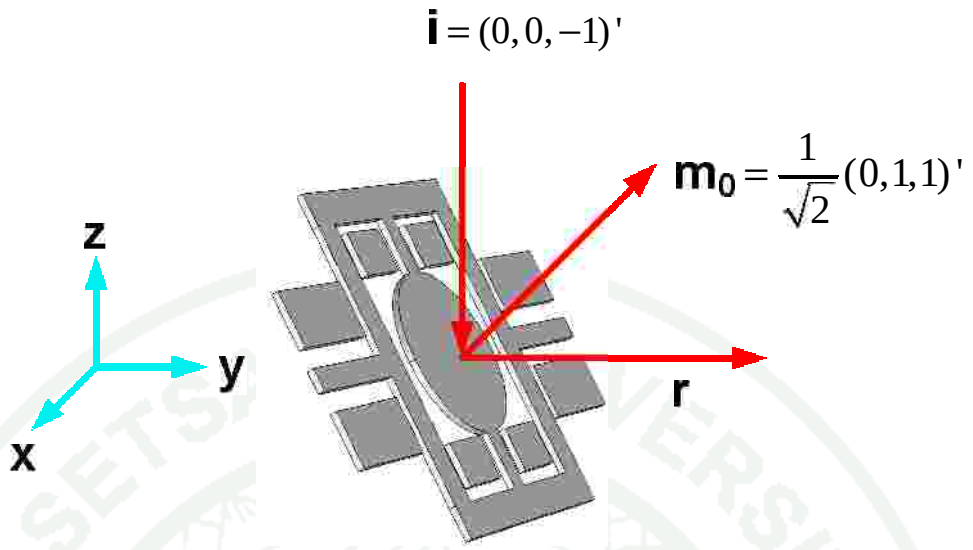

Figure 31 Optical system modeling.

Light deflected angle (θ_{op}) can be archived by using property of dot product between unit vector of y axis and vector of reflect light, always unit vector.

$$\mathbf{r} \bullet \hat{\mathbf{y}} = |\mathbf{r}||\hat{\mathbf{y}}| \cos \theta_{op}$$

$$\mathbf{r} \bullet \hat{\mathbf{y}} = \cos \theta_{op}$$

$$\theta_{op} = \cos^{-1}(\mathbf{r} \bullet \hat{\mathbf{y}}) \qquad (22)$$

where $\hat{\mathbf{y}}$ is unit vector of y axis. According to (22) and (12), the displacement distance from center due to 2D MEMS scanner rotation can be archived in Figure 32.

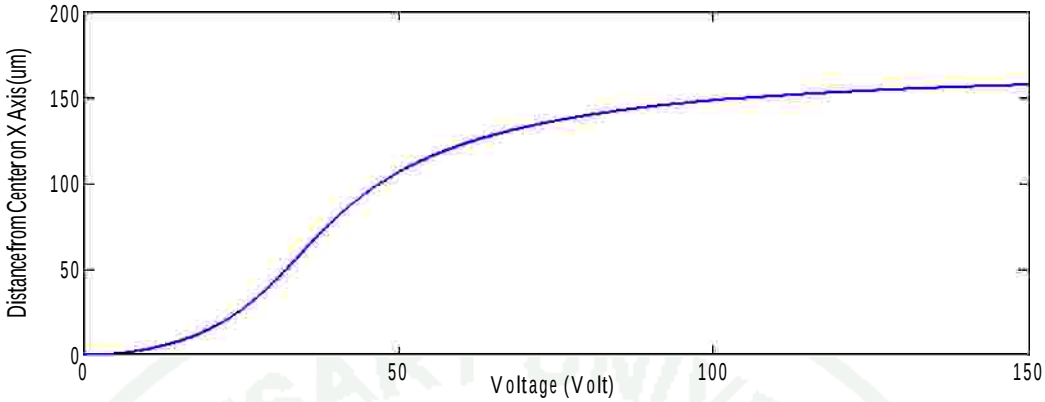

(a)

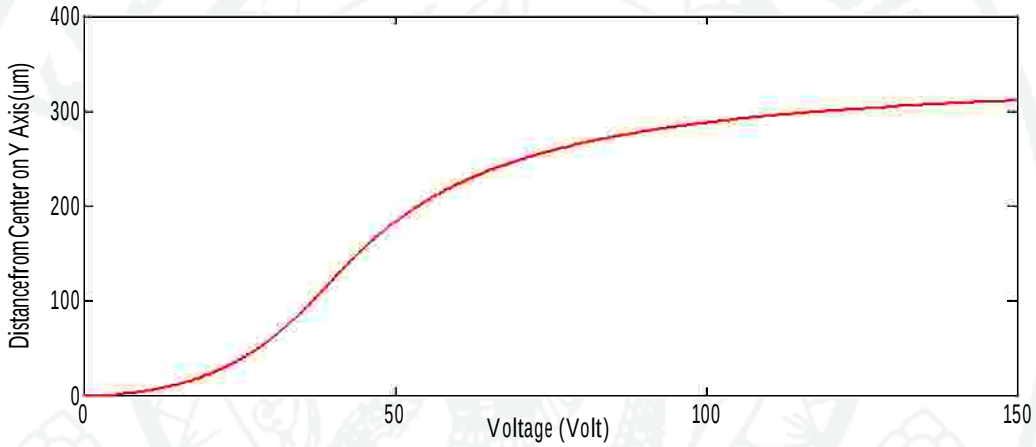

(b)

Figure 32 Displacement distance of spot on image plane (a) Inner mirror, (b) Outer frame.

3. Linearization with RBF Neural Network

The idea of linearization with RBF neural network is i lustrated in Figure 33. Four controlling voltages, V_{cx+}, V_{cx-}, V_{cy+}, *and* V_{cy-} are mapped to the expected displacement of spot on image plane, d_{x+}, d_{x-}, d_{y+}, and d_{y-}, linearly. The compensated voltages from RBF neural network, V_2, V_3, V_4, and V_5, are fed to 2D MEMS scanner model then the mechanical rotating angle from 2D MEMS scanner model will be fed to single axis confocal microscope probe to produce the displacement of spot on image plane.

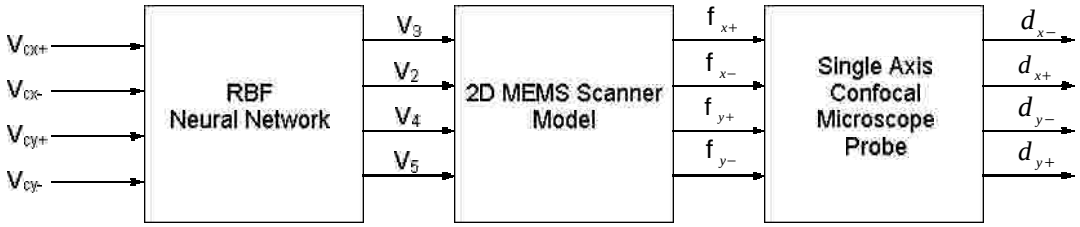

Figure 33 Schematic of the linearization with RBF neural network.

The controlling voltages linearly relate to expected displacement of spot on image plane in (23).

$$\begin{pmatrix} d_{x-} \\ d_{x+} \\ d_{y-} \\ d_{y+} \end{pmatrix} = \begin{pmatrix} k_{x+} & 0 & 0 & 0 \\ 0 & k_{x-} & 0 & 0 \\ 0 & 0 & k_{y+} & 0 \\ 0 & 0 & 0 & k_{y-} \end{pmatrix} \begin{pmatrix} V_{cx+} \\ V_{cx-} \\ V_{cy+} \\ V_{cy-} \end{pmatrix} \tag{23}$$

where k_{x+}, k_{x-}, k_{y+}, *and* k_{y-} are linear constant. These constants are determined by the following formulas:

$$k_{x+} = \frac{|\Delta d_{x-}|}{\Delta V_{cx+}} \tag{24}$$

$$k_{x-} = \frac{|\Delta d_{x+}|}{\Delta V_{cx-}} \tag{25}$$

$$k_{y+} = \frac{|\Delta d_{y-}|}{\Delta V_{cy+}} \tag{26}$$

$$k_{y-} = \frac{|\Delta d_{y+}|}{\Delta V_{cy-}} \tag{27}$$

where ΔV_{cx+}, ΔV_{cx-}, ΔV_{cy+}, *and* ΔV_{cy-} are range of controlling voltage on each axis. The positive range of analog output from data acquisit card, range from 0 to 10 V, is used to be controlling voltage so that $\Delta V_{cx+} = \Delta V_{cx-} = \Delta V_{cy+} = \Delta V_{cy-} = 10\ V$. The 2D MEMS scanner structure of V_2(X+ axis) same as V_3(X- axis) and V_4(Y- axis) same as V_5(Y+ axis) so that $k_{x+} = k_{x-} = k_x$ and $k_{y+} = k_{y-} = k_y$. From calculation result in 2D MEMS scanner characteristic simulation, law of light reflection in vector form in (20), and linear relationship of single axis confocal microscope probe in (12) the

maximum displacement for inner mirror (V_2 and V_3) is 157.58 µm at 150 V and for outer frame (V_4 and V_5) is 310.58 µm at 150 V so:

$$k_x = k_{x+} = k_{x-} = \frac{|\Delta d_{x-}|}{\Delta V_{cx+}} = \frac{157.58}{10} = 15.758 \ \mu m / volt \tag{28}$$

$$k_y = k_{y+} = k_{y-} = \frac{|\Delta d_{y-}|}{\Delta V_{cy+}} = \frac{310.46}{10} = 31.046 \ \mu m / volt \tag{29}$$

The linear relationship between controlling voltage and displacement of spot on image plane are shown in Figure 34.

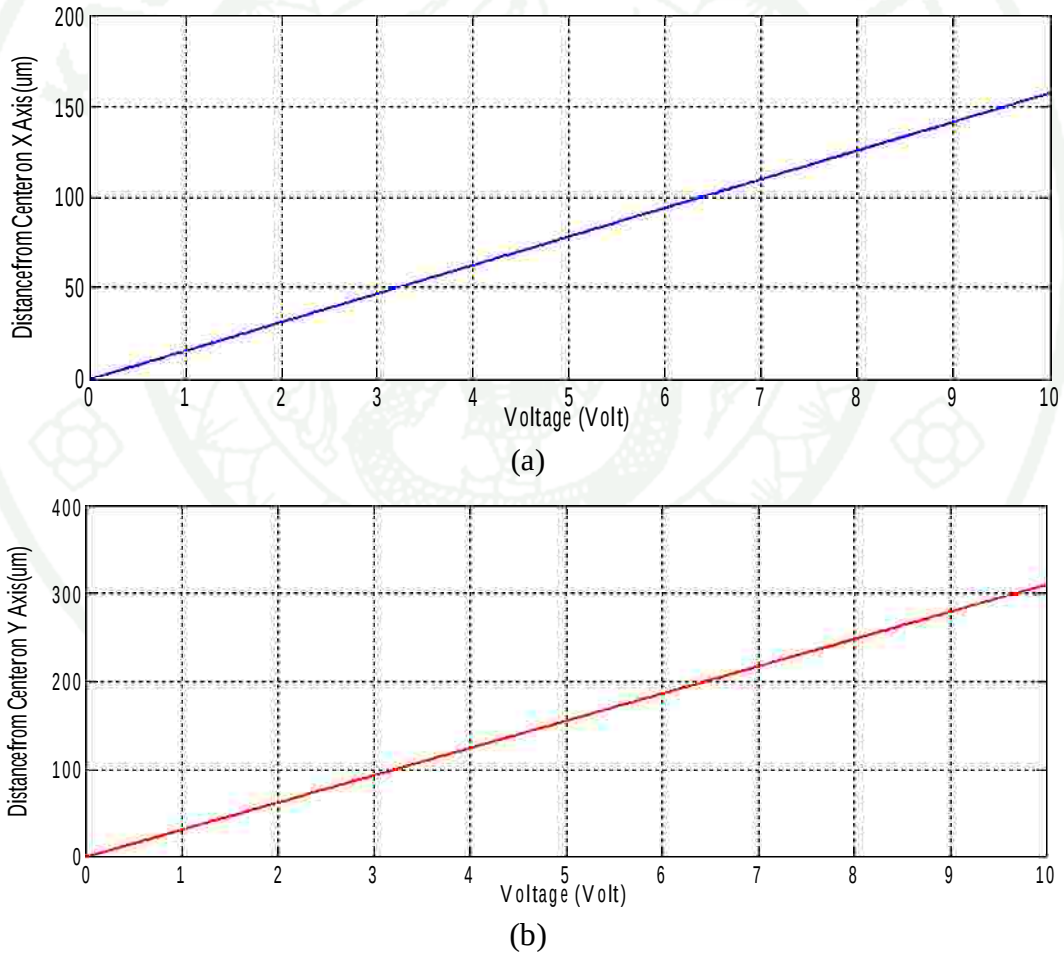

Figure 34 Linear relationship of controlling voltages and displacement of spot on image plane (a) Inner mirror, (b) Outer frame.

3.1 Radial Basis Neural Network Training

The RBF neural network (Powell 1985) is a fully connected feedforward neural network with one hidden layer and an output layer. There are three tiers in the network as shown in Figure 35: input layer (source nodes), hidden layer (to implement a radial activated function) and the output (to respond to the input). Their excellent approximation capabilities have been studied in (Poggio and Girosi, 1990; Park and Sandberg, 1991). Due to their nonlinear approximation properties, RBF networks are able to model complex mappings, which perceptron neural networks can only model by mean of multiple intermediary layers (Haykin, 1994). The input into an RBF neural network is nonlinear while the output is linear. Each nodes of hidden layer implement Gaussian density function as its radial basis function while each of output nodes implements weighted sum of hidden node outputs.

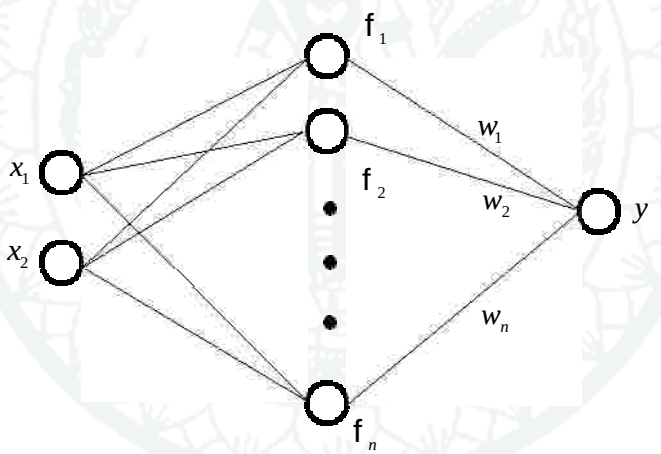

Figure 35 Radial Basis Function Neural Network architecture.

The RBF function $\mathsf{f}_i(x)$ of an i^{th} hidden node is Gaussian Radial Basis Function which is defined as:

$$\mathsf{f}_i(x-c_i) = \exp\left(-\frac{\|x-c_i\|^2}{2\mathsf{s}^2}\right) \tag{30}$$

where c_i is the center of i^{th} hidden node, $\|x-c_i\|$ is Euclidian distance between input and center of hidden node, and s is the Gaussian curve's width of the i^{th} center.

The output function of RBF neural network is given by:

$$y_j(x) = \sum_{i=1}^{N} w_{ij} \mathrm{f}\ (x_j - c_i) + w_{i0} \tag{31}$$

where $y_j(x)$ is j^{th} output node, N is number of hidden node, w_{ij} is weight between i^{th} hidden node and j^{th} output node.

The neural network model underlies the function of a certain mapping. In order to model such a mapping, the network weights and topology have to be found. There are two categories of training algorithms: supervised and unsupervised. RBF neural networks are used mainly in supervised applicat In supervised applications, a set of data samples called training set which the corresponding network outputs are known is provided. In this case the network parameters are found such that they minimize the mean square error (MSE) function:

$$E = \frac{1}{N} \sum_{j=0}^{N-1} [t_j^n - y_j(x^n)]^2 \tag{32}$$

where x^n is the input samples, N is number of samples, and t_j^n is the output of input samples.

The Radial Basis neural network is already a function MATLAB that has structure in Figure 36. Radial basis neural networks consist of two layers: a hidden radial basis layer with S^1 neurons and an output linear layer with S^2 neurons. Input vector **p** and center matrix $\mathbf{IW}^{1,1}$ are fed to || dist || box to produces a vector set having S_1 elements. These elements are the Euclidian distance between the input vector and center vectors ${}_i\mathbf{IW}^{1,1}$. The bias vector $\mathbf{b}^1$ multiply element by element with the output of || dist ||. The output of the first layer will be through Linear Layer to produce output $\mathbf{a}^2$ vector.

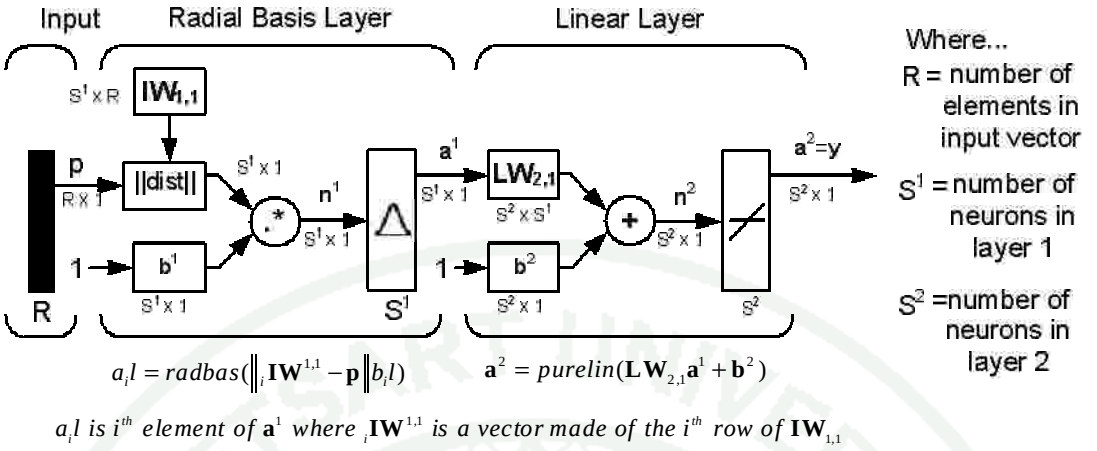

Figure 36 Radial Basis neural network in MATLAB.

The data set for training RBF neural network is created via the process in Figure 37. The corresponding mechanical angles are calculated in analytic model by using input the compensated voltages from 0 to 150 V, stepping 0.2 V. Then, the optical deflected angles are calculated by using law of light reflection. The controlling voltages that are input to neural network are calculated by relationship between displacement distance from center on image plane and controlling voltages. Therefore, the data set for training RBF neural network consists of controlling voltage and compensated voltages from analytical calculation which have 601 sample pair. Refer to Figure 33, the controlling voltages are **R** and compensated voltages will be $\mathbf{a}^2$ in Figure 36. However, the accuracy of neural network on number of hidden nodes so; the MSE limit is adjusted for proper number hidden nodes which can be used in the application. For inner mirror and outer frame, we created three neural networks with difference MSE limit that cause difference on number of hidden nodes. Figure 38 and Figure 39 show comparison graphs between output from analytical calculation and output from neural network and graphs of neural network training process for inner mirror and outer frame, respectively. The MSE is calculated by:

$$MSE = \frac{1}{601}\sum_{i=0}^{600}(V_{com}(i) - V_{NN}(i))^2 \tag{33}$$

where $V_{com}(i)$ is i^{th} compensated voltage in sample pair and $V_{NN}(i)$ is i^{th} output voltage from neural network.

As the result, the neural network for inner mirror with 252 hidden nodes has MSE equals 0.258352, with 253 hidden nodes has MSE equals 0.08571 , and with 332 hidden nodes has MSE equals 0.0454915. For outer frame, the neural network with 15 hidden nodes has MSE equals 0.175941, with 16 hidden nodes has MSE equals 0.0969679, and with 25 hidden nodes has MSE equals 0.0380706.

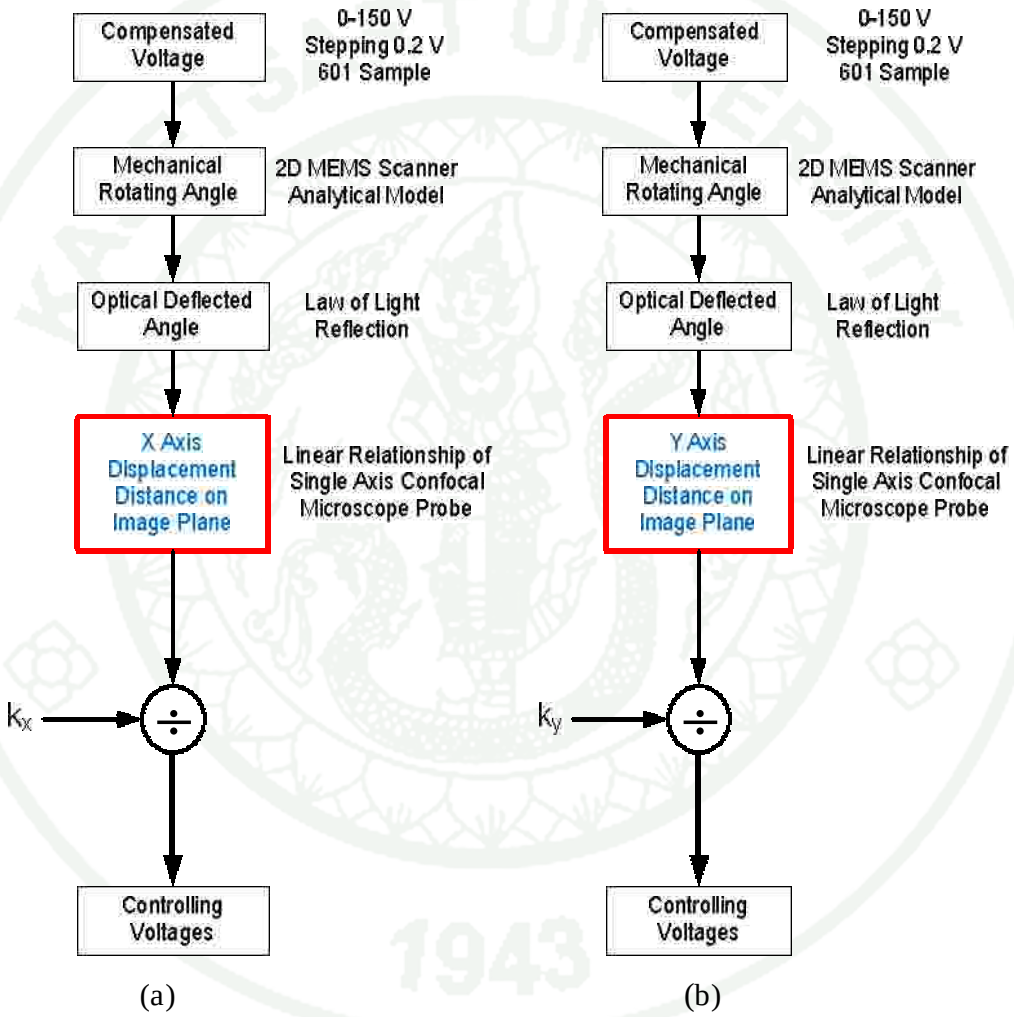

Figure: 37 Training data set creation (a) Inner mirror (b) Outer frame.

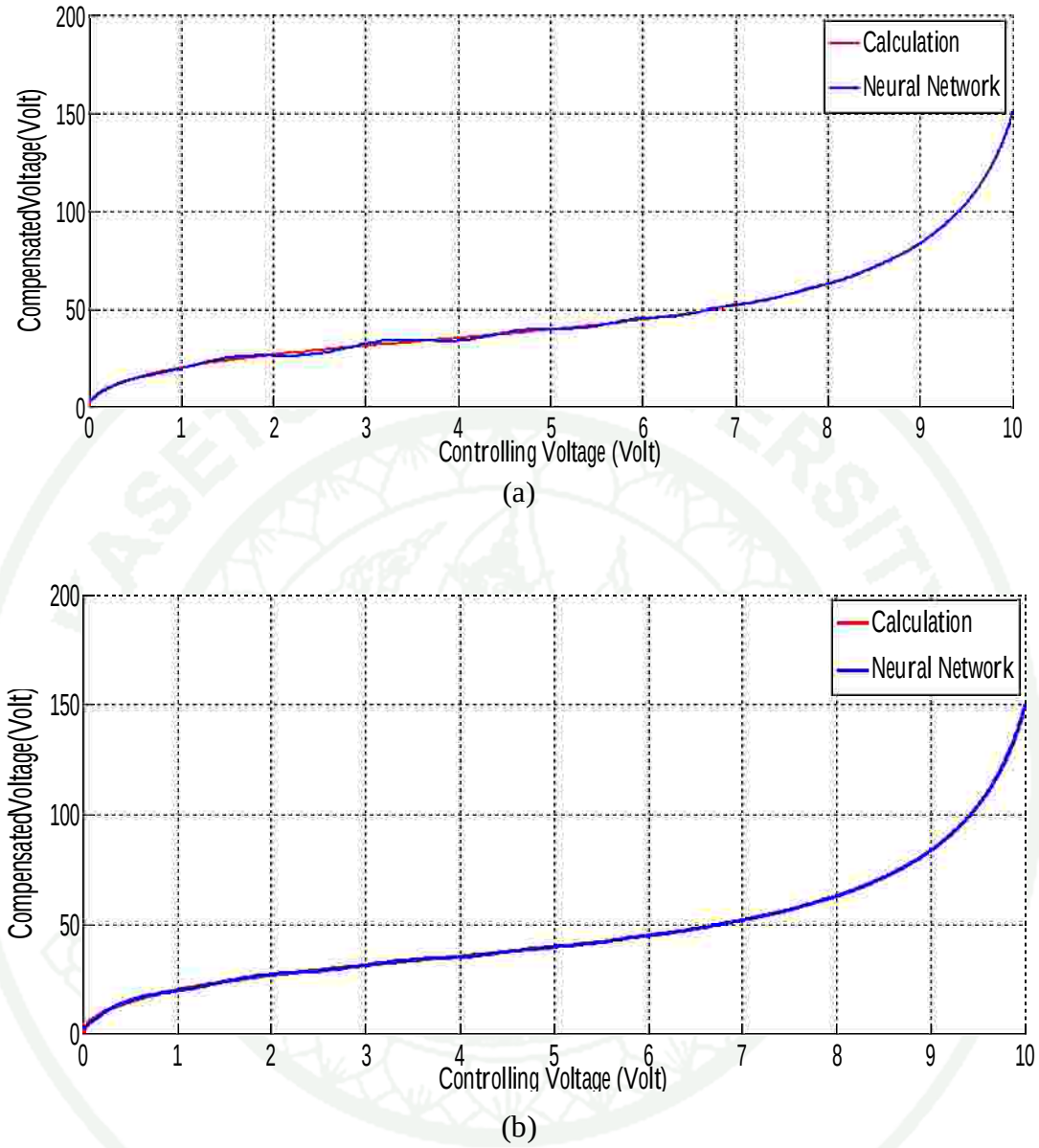

Figure 38 Comparison graph between output from analytical calculation (red line) and output from neural network (blue line) for inner mirror (a) 252 hidden nodes (MSE = 0.258352), (b) 253 hidden nodes (MSE = 0.0857152), (c) 332 hidden nodes (MSE = 0.0454915), (d) Number of hidden nodes versus MSE in neural network training process for inner mirror.

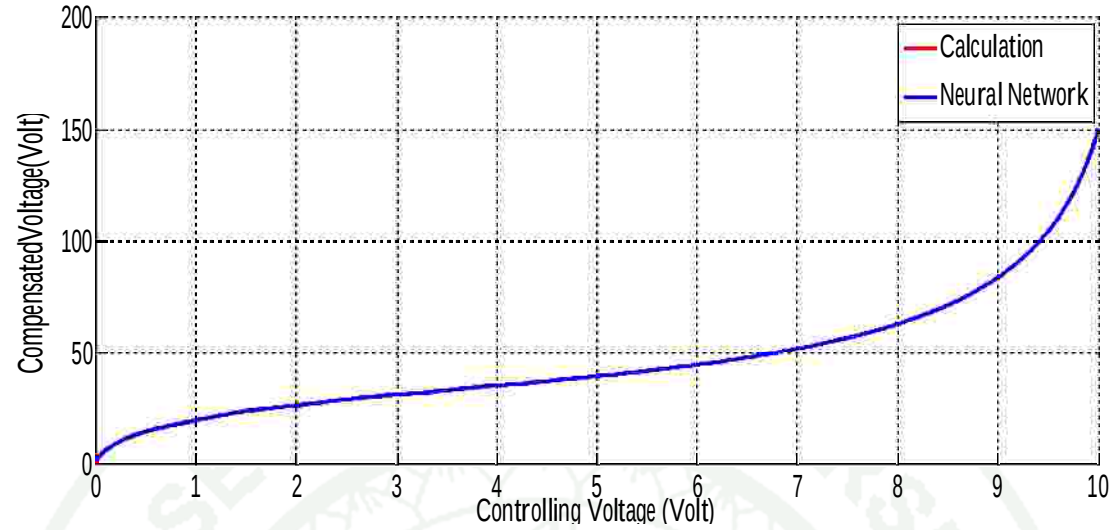

(c)

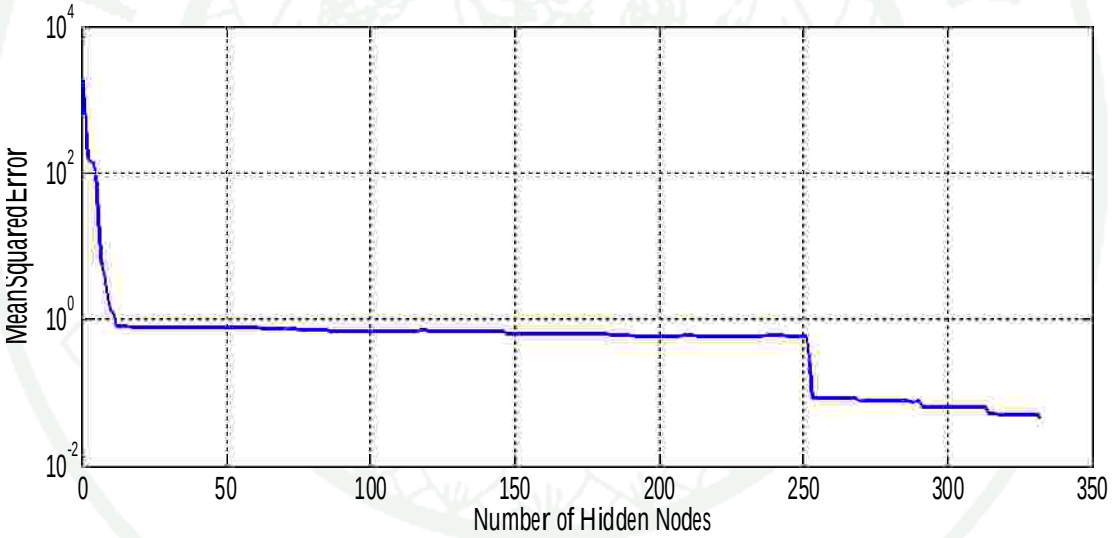

(d)

Figure 38 (Continued).

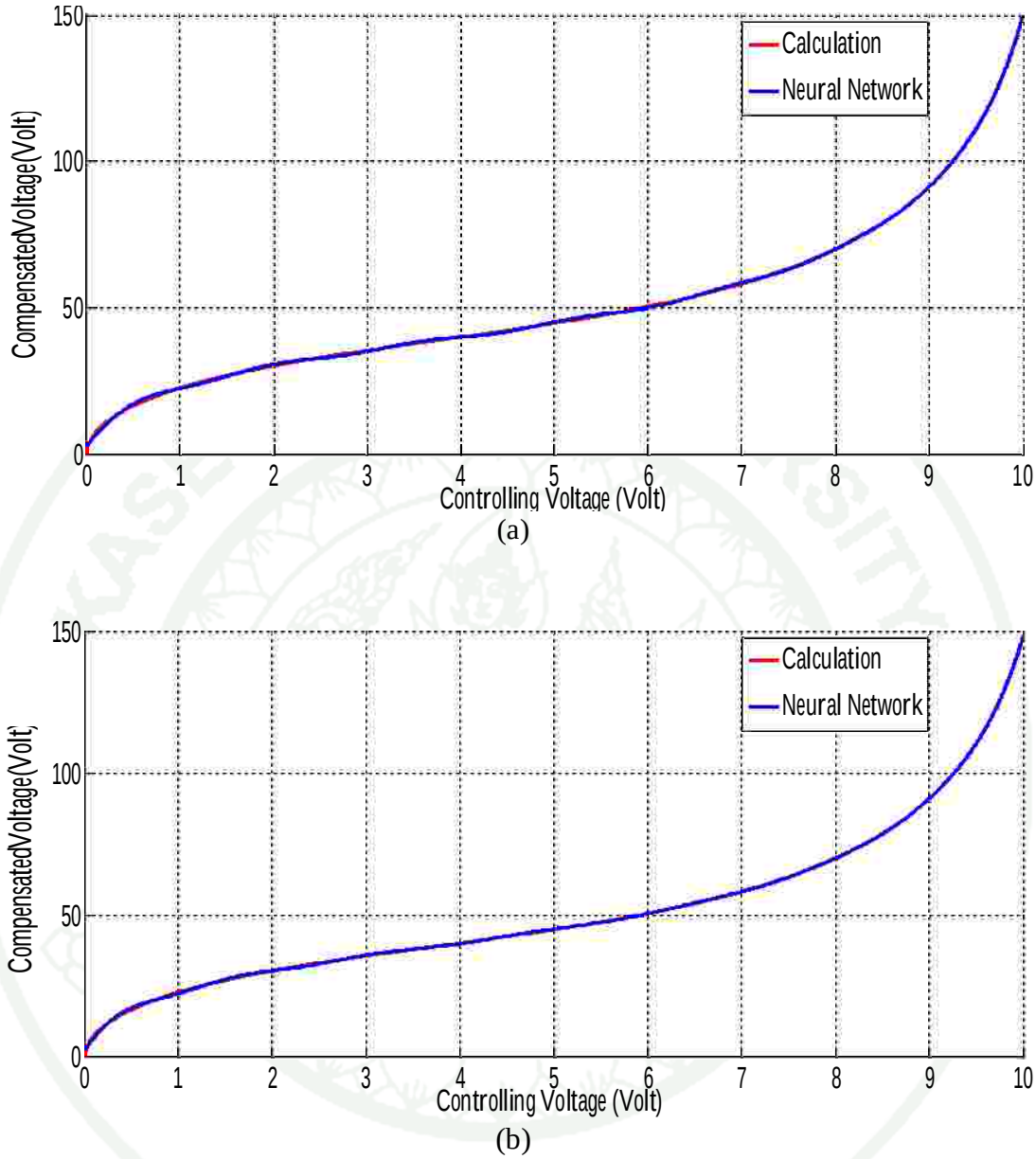

Figure 39 Comparison graph between output from analytical calculation (red line) and output from neural network (blue line) for outer frame (a) 15 hidden nodes (MSE = 0.175941), (b) 16 hidden nodes (MSE = 0.0969679), (c) 25 hidden nodes (MSE = 0.0380706), (d) Number of hidden nodes versus MSE in neural network training process for outer frame.

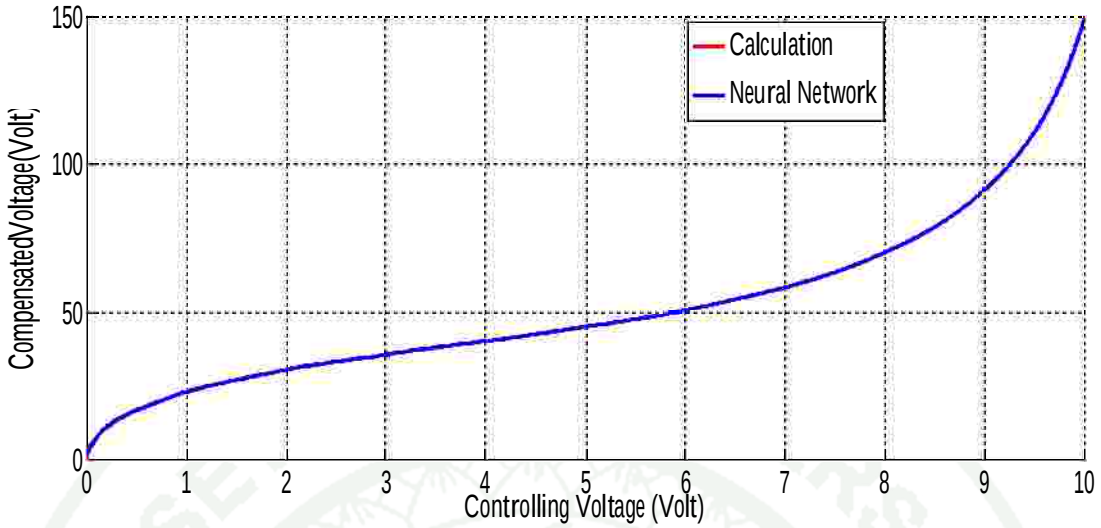

(c)

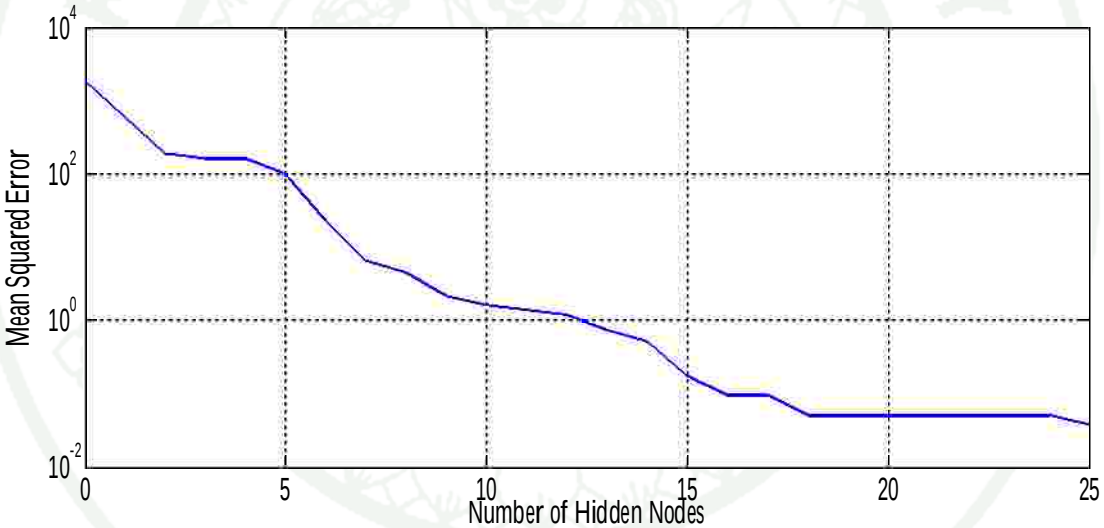

(d)

Figure 39 (Continued).

3.2 Two Points Resolution

The ability to separate the two closest illumination points will determine the resolving power of an imaging device. Therefore, the definition of resolution is the minimum distance between distinguishable of two illumination points in an image. The Rayleigh definition is often stated in the form: two points of equal brightness can be distinguished if there is a 26.5% dip in intensity between them (T. R. Corle and G. S. Kino, 1996). This definition corresponds to the two illumination points for confocal microscope being separated by a distance d_c(Rayleigh)(T. R. Corle and G. S. Kino, 1996), defines as

$$d_c(Rayleigh) = \frac{0.56\lambda}{NA} \tag{34}$$

where λ is wavelength and NA is numerical aperture. So, the minimum distance for single axis confocal probe in this thesis occur when $\lambda = 488\ nm$. Thus:

$$d_c(Rayleigh) = 1.301\ \mu m .$$

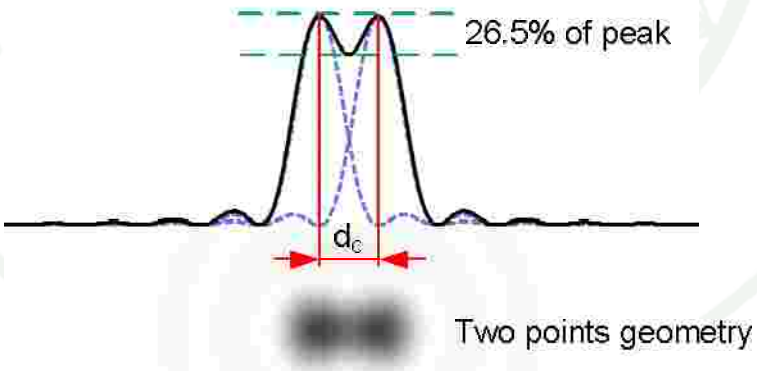

Figure 40 Point spread function of two illumination points separated with Rayleigh distance.

According to Rayleigh definition, the error distance cause from neural network, difference between actual position and expected position on image plane, is limited by Rayleigh distance.

RESULT AND DISCUSS

Result

The performance of neural network is measured by comparing the displacement distances with respect to center of image plane which result from analytical calculation and neural network. The testing process is depicted in Figure 41. The compensated voltages from 0 to 150 V, stepping 0.3V, are fed to 2D MEMS scanner model to create the corresponding mechanical rotating angles. Then, the optical deflected angles are calculated by supplying mechanical rotating angles from previous stage through law of light reflection. After that, the displacement distances of analytical calculation are resulted by sourcing the optical deflected angles to linear relationship of single axis confocal microscope probe.

On the other hand, the neural network is inputted by controlling voltages. These controlling voltages are archived by supplying displacement distances through linear mapping of displacement distance and controlling voltage in (28) or (29). Then, the neural network computes compensated voltages corresponding to controlling voltages. According to compensated voltages from previous stage, the displacement distances are calculated by using 2D MEMS scanner model, law of light reflection, and linear relationship of single axis confocal microscope probe, likely displacement distances form analytic calculation method.

Finally, the distance errors are calculated by comparing between displacement distances from analytic calculation and neural network. Figure 42 and Figure 43 show the errors of displacement distances from analytical calculation and neural network.

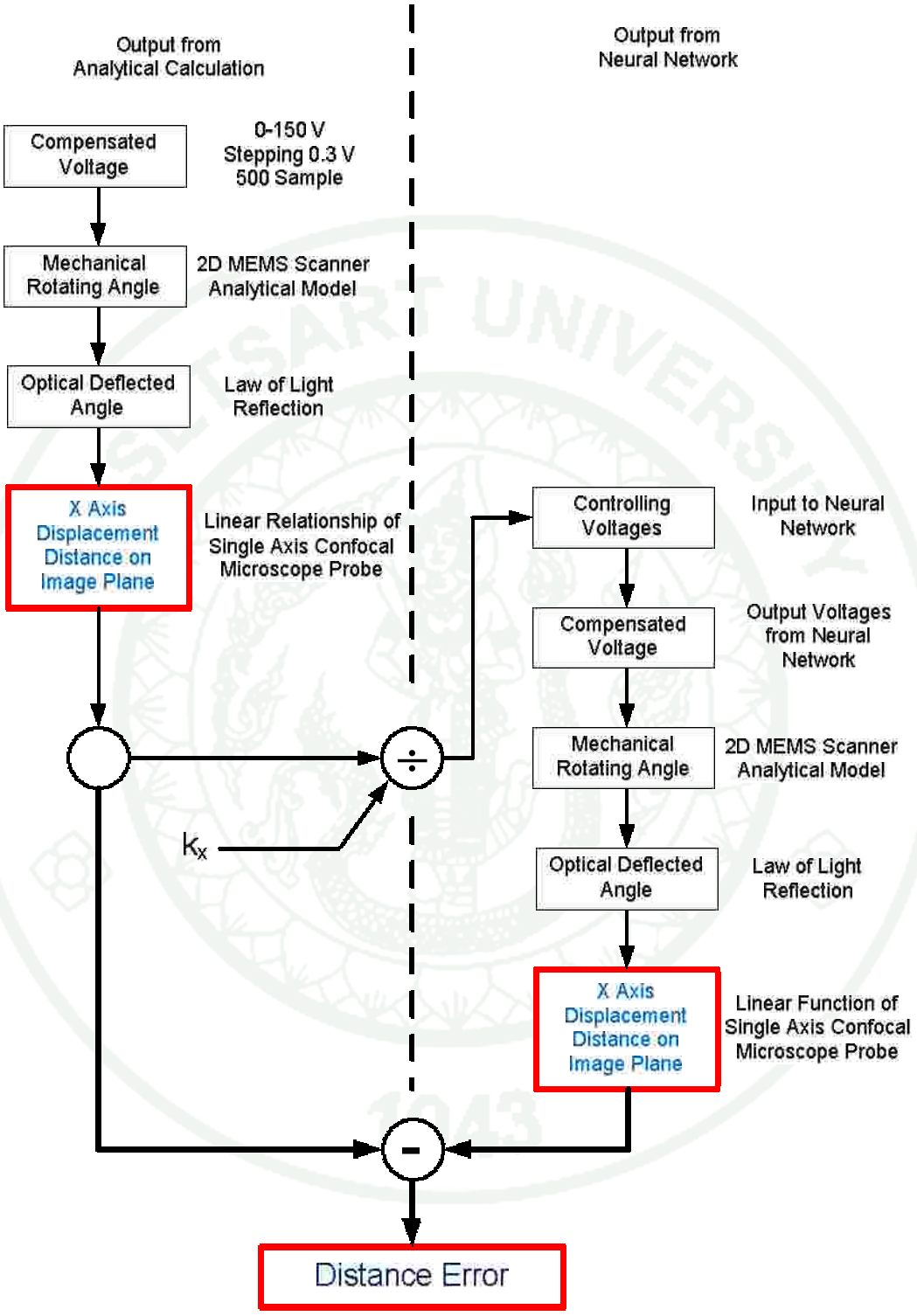

(a)

Figure 41 Test process diagram (a) Inner mirror, (b) Outer frame.

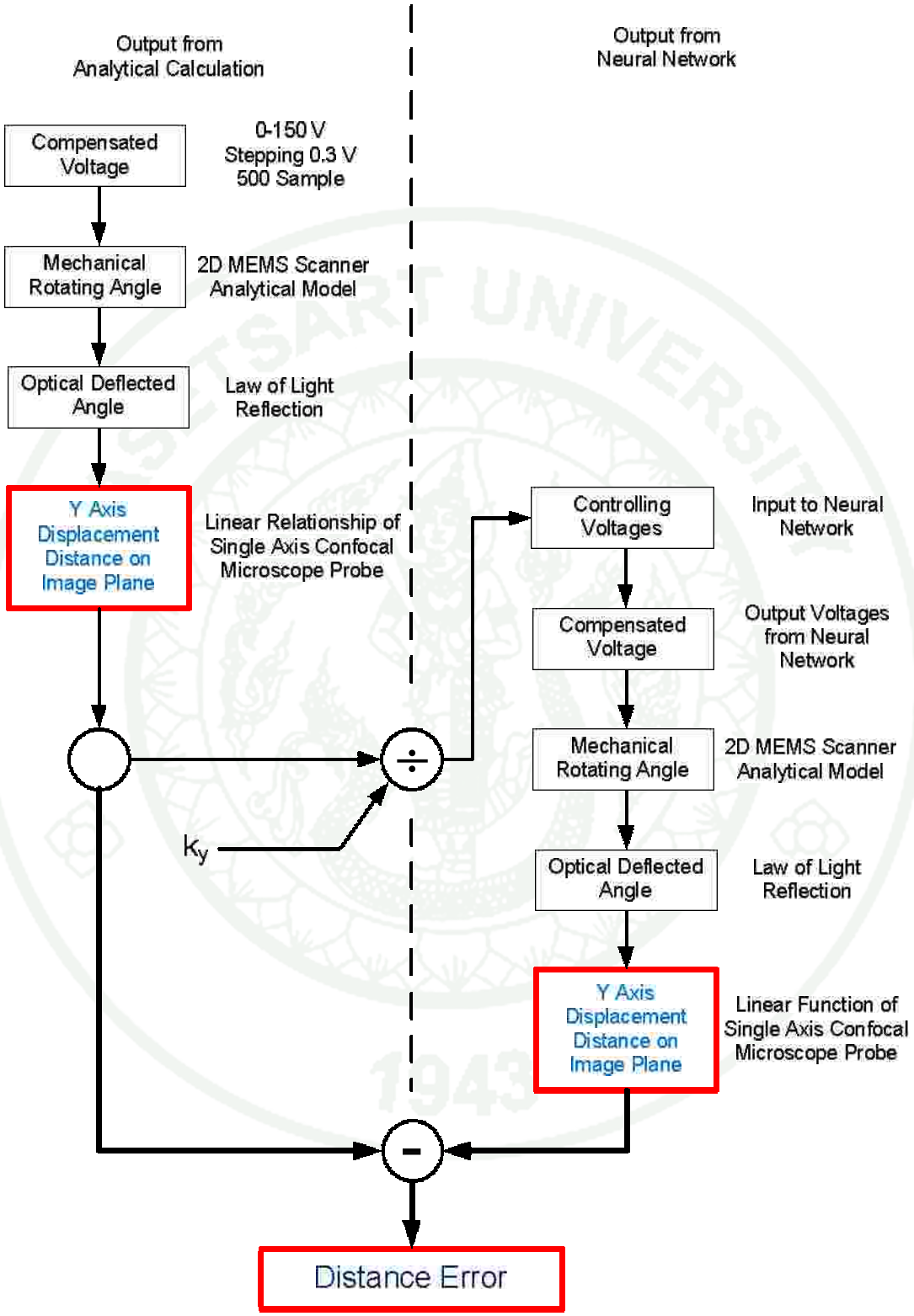

(b)

Figure 41 (Continued).

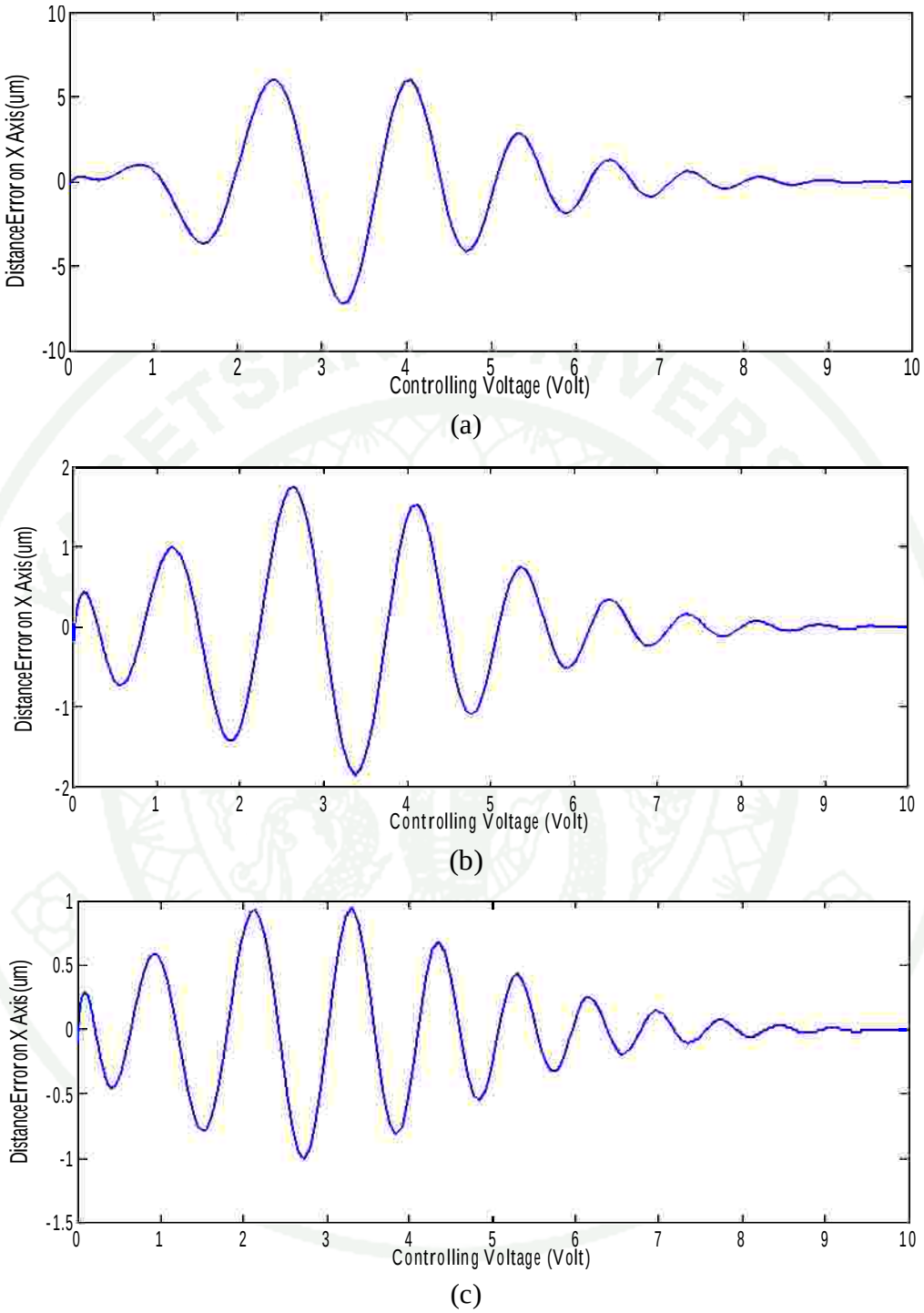

Figure 42 The distance error of inner mirror (a) 252 hidden nodes, (b) 253 hidden nodes, (c) 332 hidden nodes.

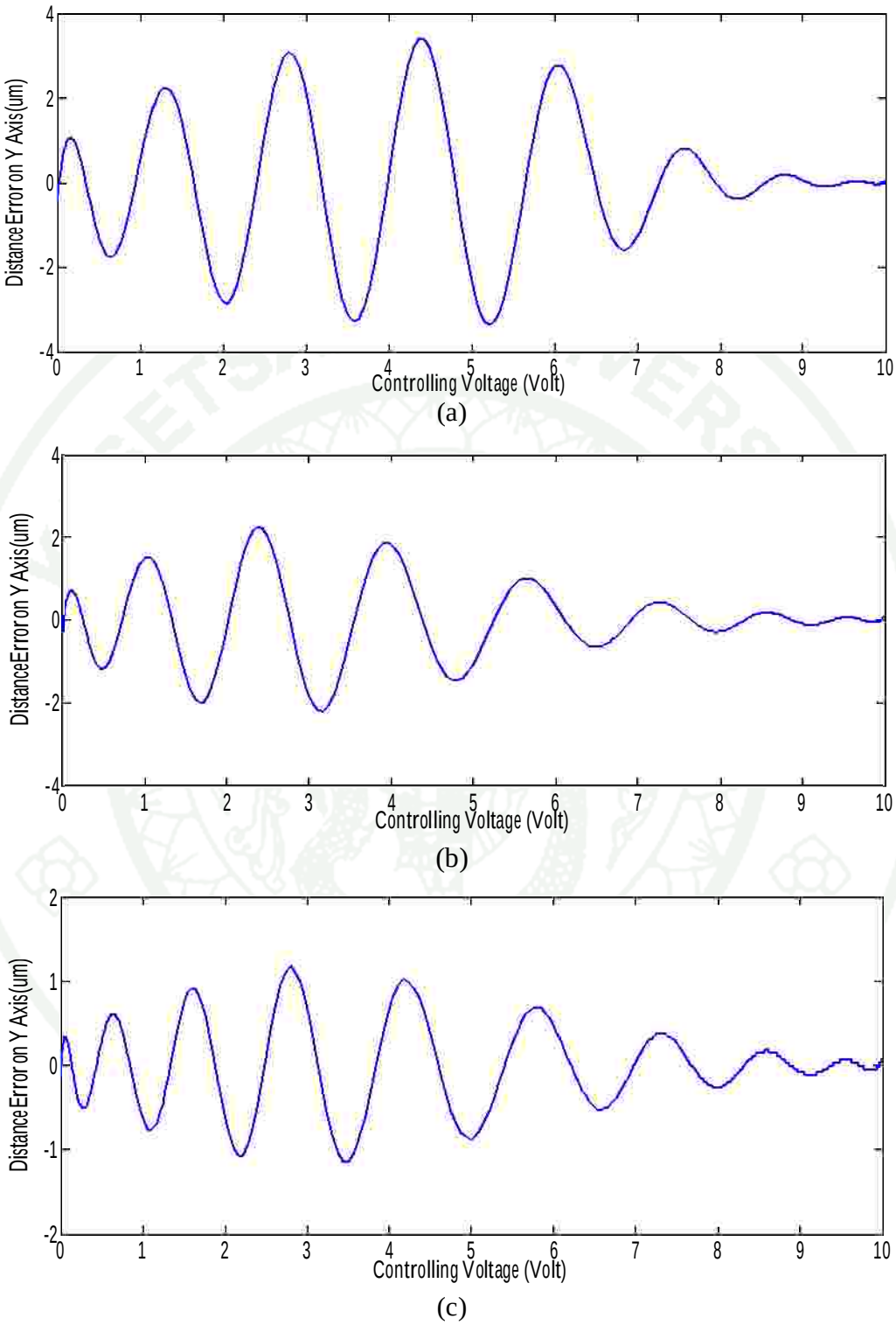

Figure 43 The distance error of outer frame (a) 15 hidden nodes, (b) 16 hidden nodes, (c) 25 hidden nodes

Discussion

The MEMS based single axis confocal microscope inherently suffers from nonlinear scanning field. This defect calls for linearization to improve the system performance. The proposed linearization with RBF neural network presents the ability to reduce the effect of nonlinear scanning field due to 2D MEMS scanner operation. According to displacement distances calculated form neural network outputs for inner mirror, the maximum distance error of neural network with 252 hidden nodes and 253 hidden nodes are more than Rayleigh distance while the neural network which has 332 hidden nodes and MSE in training process equals 0.0454915 results maximum distance error less than Rayleigh distance. Meanwhile, the maximum distance error of displacement distances calculated form neural network outputs for outer frame with 15 hidden nodes and 16 hidden nodes are more than Rayleigh distance while the neural network with 25 hidden nodes and MSE in training process equals 0.0380706 results maximum distance error less than Rayleigh distance.

In summary, the RBF neural network for inner mirror and outer frame that has MSE in training process less than 0.05 can be models to control 2D MEMS scanner in MEMS based single axis confocal microscope. However, the proposed linearization with RBF neural network cannot completely overcome the nonlinear scanning field due to 2D MEMS scanner operation because there still are errors, indicating by MSE, in neural network.

CONCLUSION AND RECOMMENDATION

Conclusion

A miniature single axis confocal microscope probe is usually designed to use with only one wavelength. An essential problem when a iniature single axis confocal microscope probe is used other wavelengths, it causes chromatic focal shift on image. A purpose of this study, there are two proposes, is to propose a design to counteract this negative effect. To reduce the effect chromatic focal shift, the property of achromatic lens is considered. In this research, a miniature single axis confocal microscope probe for multiple wavelengths is designed with three achromatic lenses. The design archives axial focal shift, covering wavelength from 488 nm to 785 nm, inward of 2.56 μm for wavelength 488 nm and outward of 5.96 μm for wavelength 785 nm, centering at wavelength 635 nm. This design obtains 0.21 NA.

A 2D MEMS scanner is deployed for light deflection in MEMS based single axis confocal microscope. But the nonlinearity of MEMS scanner operation distorts scanning field. Another purpose of this study is to propose a method to improve the nonlinearity of scanning field. To obtain a linearized scanning field, RBF neural network is implied to control the rotation of MEMS scanner via controlling voltage. Each of RBF neural networks is created from 601 input-output pairs, data set, generated from 2D MEMS scanner characteristic simulation. Then, Each of RBF neural networks is tested with 501 inputs, test set, which are different from data set. The compensated voltages which are output from neural will be calculated the displacement distance with respect to center of image plane. The different values between displacement distances calculated from neural network utput and displacement distances calculated from analytical calculation are distance errors on scanning field.

Two points resolution definition is implied to limit the maximum distance error. As a result, the RBF neural networks for inner and outer frame that has MSE in training process less than 0.05 can be models to control MEMS scanner in MEMS based single axis confocal microscope.

Recommendation

The following topics, arising out of this thesis, seem worthy of further research.

1. Since the designing target of a miniature confocal microscope probe for multiple wavelengths in this thesis is to reduce chromatic aberration but is not included to improve image resolution. The next natural step is to increase the numerical aperture for better image resolution.

2. Since all neural networks have to use data set from 2D MEMS characteristic simulation therefore the actual 2D MEMS scanner's performance has to correspond with characteristic simulation. To archive condition, 2D MEMS scanner design, MEMS fabrication processes, and MEMS fabrication techniques must be developed further.

3. Since the linearization method with RBF neural network is not limited to MEMS based single axis confocal microscope, it could be interesting to apply it to other MEMS based devices which also suffer from nonlinearity.

4. Since the RBF neural networks in this thesis use data from 2D MEMS scanner characteristic simulation but the data set from practical experiment may contain interference. For realistic simulation, the data set could be included some noise. To support that situation the RBF neural network's performance will be further development for practical implementation.

5. Since the RBF neural network will have more hidden nodes if it is expected to have more accuracy that will increases the complexity of neural network. To decrease the complexity of neural network, the low-weight hidden nodes could be ignored while it maintains the accuracy.

LITERATURE CITED

Aguirre A. D., P. R. Herz, Y. Chen, J. G. Fujimoto, W. Piyawattanametha, L. Fan, S. T. Hsu, M. Fujino, M. C. Wu and D. Kopf. 2005. Ultrahigh resolution OCT imaging with a two-dimensional MEMS scanning endoscope, pp. 277-282. *In* **SPIE Volume 5692.**

Aribe K. A. and G. K. Knopf. 2005. Neural network control of a MEMS torsion micro mirror, pp. 737 – 74. *In* **Control Applications.**

Carr E. J., S. S. Olivier and O. Solgaard. 2005. Large-stroke self-aligned vertical comb drive actuators for adaptive optics applications, pp. 61130O-61130O-9. *In* **Proceedings of SPIE Volume 6113.**

Chantakien T., P. Raphisak, I. Kumazawa and W. Piyawattanametha. 2011. Design and simulate of MEMS based confocal microscope probes. **International Conference of Information and Communication Technology for Embedded Systems**

Chantakien T., P. Raphisak, I. Kumazawa and W. Piyawattanametha. 2011. MEMS-based handheld single-axis confocal microscope design and experiment, pp. 38-41. *In* **8th International Conference on Electrical Engineering/ Electronics, Computer, Telecommunications and Information Technology.**

Chao F., S. He, J. Chong, R. B. Mrad and L. Feng. 2011. Development of a micromirror based laser vector scanning automotive HUD, pp. 75-79. *In* **Mechatronics and Automation (ICMA)**.

Chu P. K., W. Piyawattanametha and T. D. Wang. 2010. Miniature Dual Axes Confocal Microscope for Real Time In Vivo Imaging, pp. 393-427. *In* **Advances in Solid State Circuits Technologies.**

Chung H.-Y. and R. Chen. 2005. Characterization and analysis of vertically comb-driven micromirrors. **MEMS, NANO and Smart Systems.**

Corle T. R. and G. S. Kino. 1996. Confocal Scanning Optical Microscopy and Related Imaging Systems. *In* **Academic Press, Inc.**

Dickensheets D. L. and G. S. Kino. 1996. Micromachined scanning confocal optical microscope, pp. 764-766. *In* **Optic Letter Volume 21.**

Dickensheets D. L. and G. S. Kino. 1998. Silicon-micromachined scanning confocal optical microscope, pp. 38-47. *In* **Journal of Microelectromechanical Systems Volume 7.**

Dickensheets D. L. 2001. MOEMS-based instruments for in-situ scanning confocal microscopy, pp. 68-69. *In* **Lasers and Electro-Optics Society.**

Dwyer P. J., C. A. DiMarzio, J. M. Zavislan, W. J. Fox and M. Rajadhyaksha. 2006. Confocal reflectance theta line scanning microscope for imaging human skin in vivo, pp. 942-944. *In* **Optics Letter Volume 31.**

Hagelin P. M. and O. Solgaard. 1999. Optical raster-scanning displays based on surface-micromachined polysilicon mirrors, pp. 67 - 74. *In* **IEEE Journal of Selected Topics in Quantum Electronics Volume 5.**

Hah D., P. R. Patterson, H. D. Nguyen, H. Toshiyoshi and M. C. Wu. 2004. Theory and experiments of angular vertical comb-drive actuators for scanning micromirrors, pp. 505-513. *In* **IEEE Journal of Selected Topics in Quantum Electronics Volume 10.**

Haykin S. 1994. Neural Networks: Acomprehensive Foundation. In **Upper Saddle River, NJ: Prentice Hall.**

Hofmann U., S. M., R. Schütz, K. Dörschel, B. Wagner and M. Witt. 1999. Electrostatically driven micromirrors for a miniaturized confocal laser scanning microscope, pp. 29-38. *In* **Society of Photo-Optical Instrumentation Engineers.**

Hoy C. L., O. Ferhanolu, M. Yildirim, W. Piyawattanametha, H. Ra, O. Solgaard and A. B.-Yakar. 2011. Optical design and imaging performance testing of a 9.6-mm diameter femtosecond laser microsurgery probe, pp. 10536-1055. *In* **Optics Express Volume 19.**

Jung W., S. Tang, T. Xie, D. T. McCormick, Y.-C. Ahn, J. Su, I. V. Tomov, T. B. Krasieva, B. J. Tromberg and Z. Chen. 2008. Miniaturized probe using dual axis MEMS scanner for endoscopic multiphoton excitation microscopy, pp. U48-U54. *In* **Endoscopic Microscopy III Volume 6851.**

Kiang M.-H., O. Solgaard, R.S. Muller and K.Y. Lau. 1996. Micromachined polysilicon microscanners for barcode readers, pp. 1707 – 1709. *In* **IEEE Photonics Technology Letters Volume 8.**

Knittel J., L. Schnieder, G. Buess, B. Messerschmidt and T. Possner. 2001. Endoscope-compatible confocal microscope using a gradient index-lens system, pp. 267-273. *In* **Optics Communications.**

Kumar K., K. Hoshino, H.-J. Shin, R. R.-Kortum and X. Zhang. 2006. High-Reflectivity Two-Axis Vertical Comb Drive Microscanners for Confocal Imaging Applications, pp. 120 - 121. *In* **Conference on IEEE/LEOS Optical MEMS and Their Applications.**

Liu J. T. C., M. J. Mandella, N. O. Loewke, H. Haeberle, H. Ra, W. Piyawattanametha, O. Solgaard, G. S. Kino and C. H. Contag. 2010. Micromirror-scanned dual-axis confocal microscope utilizing a gradient-index relay lens for image guidance during brain surgery, pp. 026029-026025. *In* **Journal of Biomedical Optics.**

Maitland K. C., H. J. Shin, H. Ra, D. Lee, O. Solgaard and R. R.-Kortum. 2006. Single fiber confocal microscope with a two-axis gimbaled MEMS scanner for cellular imaging, pp. 8604-8612. *In* **Optics Express Volume 14.**

Milanovic V. 2007. Improved Control of the Vertical Axis Scan for MEMS Projection Displays, pp. 89-90. *In* **Optical MEMS and Nanophotonics.**

Milanovic V., K. Castelino and D. T. McCormick. 2007. Highly adaptable MEMS-based display with wide projection angle, pp. 143 – 146. *In* **Micro Electro Mechanical Systems.**

Milanovic V. 2009. Linearized Gimbal-Less Two-Axis MEMS Mirrors. *In* **Optical Society of America.**

Ode T. 1994. A new technique for optical 3D measurements with a confocal scanning laser microscope, pp. 672 - 676. *In* **Conference on Instrumentation and Measurement Technology.**

Park J. and J. W. Sandberg. 1991. Universal approximation using radial basis functions network, pp. 246-257. **Neural Computation Volume 3.**

Rouse A. R. and A. F. Gmitro. 2000. Multispectral imaging with a confocal microendoscope, pp. 1708-1710. *In* **Optics Letters Volume 25.**

Piyawattanametha W., P. R. Patterson, D. Hah, H. Toshiyoshi and M. C. Wu. 2005. Surface and Bulk Micromachined Two-Dimensional Scanner Driven by Angular Vertical Comb Actuators, pp. 1329-1338. *In* **Journal of Microelectromechanical Systems Volume 14.**

Piyawattanametha W., H. Ra, M. J. Mandella, K. Loewke, T. D. Wang, G. S ino, O. Solgaard and C. H. Contag. 2009. 3-D Near-Infrared Fluorescence Imaging Using an MEMS-Based Miniature Dual-Axis Confocal Microscope, pp. 1344-1350. *In* **IEEE Journal of Selected Topics in Quantum Electronics Volume 15.**

Poggio T. and F. Girosi. 1990. Networks for approximation and learning, pp.1481-1497. *In* **Proceedings of IEEE Volume 78.**

Poland S. P., J. M. Girkin, L. Li and D. Uttamchandani. 2009. External linearisation of a MEMS electrothermal scanner with application in a confocal microscope, pp. 106 – 111. *In* **Micro & Nano Letters, IET Volume 4.**

Powell M. J. D. 1985. Radial basis functions for multivariable interpolation : a review. In Cox, M. G., and Mason, J. C. (eds.), Algorithm for the Approximation of Functions and Data. **Oxford University Press, Newyork.**

Ra H., Y. Taguchi, D. Lee, W. Piyawattanametha and O. Solgaard. 2006. Two-Dimensional MEMS Scanner for Dual-Axes Confocal in Vivo Microscopy, pp. 862-865. *In* **Micro Electro Mechanical Systems.**

Ra H., W. Piyawattanametha, Y. Taguchi, D. Lee, M. J. Mandella and O. Solgaard. 2007. Two-Dimensional MEMS Scanner for Dual-Axes Confocal Microscopy, pp. 969 – 976. *In* **Journal of Microelectromechanical Systems Volume 16**.

Shin H. J., M. C. Pierce, D. Lee, H. Ra, O. Solgaard and R. R.-Kortum. 2007. Fiber-optic confocal microscope using a MEMS scanner and miniature objective lens, pp. 9113-9122. *In* **Optics Express Volume 15.**

Tsai J.-C., L.-C. Lu, W.-C. Hsu, C.-W. Sun and M. C. Wu. 2008. Linearization of a two-axis MEMS scanner driven by vertical comb-drive actuators. **Journal of Micromechanics and Microengineering Volume 18.**

Toshiyoshi H., W. Piyawattanametha, C.-T. Chan and M. C. Wu. 2001. Linearization of electrostatically actuated surface micromachined 2-D optical scanner, pp. 205-214. *In* **Journal of Microelectromechanical Systems Volume 10.**

Trimmer W. 1989. Microrobots and micromechanical systems, pp. 267-287. *In* **Sensors and Actuators A Volume 19.**

Wang T. D., C. H. Contag, M. J. Mandella, N. Y. Chan and G. S. Kino. 2003. Dual-axes confocal microscopy with post-objective scanning and low-coherence heterodyne detection, pp. 1915-1917. *In* **Optics Letter Volume 28.**

Wilson T. and A. R. Carlini. 1987. Size of the detector in confocal imaging systems, pp. 227-229. *In* **Optics Letter Volume 12.**

Xie H. 2009. MEMS-based 3D optical microendoscopy, pp. 6703 – 6705. *In* **Engineering in Medicine and Biology Society.**

Yamada K. and T. Kuriyama. 1998. A novel asymmetric silicon micro-mirror for optical beam scanning display, pp. 110-115. *In* **Proceeding of IEEE, 11th Int. Workshop Micro Electro Mechanical Systems.**

Zhao Y., F. E. H. Tay, F. S. Chau and G. Zhou. 2005. Linearization of the scanning field for 2D torsional micromirror by RBF neural network, pp. 230-236. *In* **Sensors and Actuators A: Physical Volume 121.**

Zhou G., K. K. L. Cheo, F. E. H. Tay, and F. S. Chau. 2003. Neural network approach for linearization of the electrostatically actuated double-gimballed micromirror, pp. 164-169. *In* **Design, Test, Integration and Packaging of MEMS/MOEMS.**

CIRRICULUM VITAE

NAME : Mr. Techaniti Chantakien

BIRTH DATE : February 19, 1985

BIRTH PLACE : Samutprakan, Thailand

EDUCATION :

YEAR	**INSTITUTE**	**DEGREE/DIPLOMA**
2007	King Mongkut's Institute of Technology Ladkrabang	B.Eng. (Electronics Engineering)
2012	Kasetsart Univ.	M.Eng. (Information and Communication Technology for Embedded Systems)

POSITION/TITLE : -

WORK PLACE : -

SCHOLARSHIP/AWARDS : TAIST ICTES Master Degree Scholarship

PUBLICATIONS ICTICTES2011 and ECTICON 2011